TITLE: Fine-tuned repression of Drp1 driven mitochondrial fission primes a slow cycling stem/progenitor-like state towards accelerating neoplastic transformation of keratinocytes

AUTHORS: Spurlock B[1], Parker D[1], Basu MK[2], Hjelmeland A[3], G Sajina[3], Liu S[1], Siegal G[2], Gunter A[1], Moran A[1] and Mitra K[1]*

* corresponding author (kasturi@uab.edu)

AFFILIATION:

1. Department of Genetics, University of Alabama at Birmingham, Birmingham, Alabama 35294
2. Department of Pathology, University of Alabama at Birmingham, Birmingham, Alabama 35294
3. Department of Cell Development and Integrative Biology, University of Alabama at Birmingham,
4. Department of Biology, University of Alabama at Birmingham.

Running title:

Mitochondria based priming of stem/progenitor-like state towards driving transformation

Keywords:

Drp1, Mitochondrial fission, neoplastic stem/progenitor cells, neoplastic transformation, keratinocytes, scRNA-seq, microscopy

ABSTRACT:

The opposing processes of mitochondrial fission and fusion are emerging as crucial regulators of stem cells. Stem/progenitor cells maintaining repressed mitochondrial fission appear to be primed for self-renewal and proliferation. Here, we demonstrate the causative role of fine-tuned repression of Drp1, the master regulator of mitochondrial fission, in establishing a stem/progenitor-like state towards supporting carcinogen (TCDD) driven neoplastic transformation of keratinocytes. Fine-tuned Drp1 repression maintains small networks of fused mitochondria to sustain a unique gene-expression profile with elevated stem/progenitor cell functional markers (Krt15, Sox2 etc) and their regulators (Cyclin E). Cells with this mitochondria-primed state are slow cycling, susceptible to transformation, and when enriched by mild carcinogen exposure sustains elevated self-renewal/proliferation to form less differentiated tumors. More complete Drp1 repression sustains larger hyperfused mitochondria, represses lineage specific stem/progenitor genes and prevents transformation. Therefore, our data highlights a 'goldilocks' level of Drp1 repression that supports stem/progenitor cell dependent neoplastic transformation. Future studies would reveal if bodily stresses causing mild Drp1 repression could enrich this mitochondria-primed stem/progenitor like population in tissues making them vulnerable to neoplastic transformation.

INTRODUCTION

Mitochondria play various key roles in stem cell regulation, while their involvement is complex (Lisowski, Kannan et al., 2018)(Khacho & Slack, 2017, Zhang, Menzies et al., 2018). The critical details of mitochondrial involvement in regulation of various stem cell properties are far from clear. The master regulators of mitochondrial fission and fusion processes are emerging as crucial regulators of both embryonic and adult stem cells (Khacho & Slack, 2017, Lisowski et al., 2018)(Spurlock, Tullet et al., 2020). The Dynamin Related Protein 1 (Drp1) is the master regulator of mitochondrial fission that breaks larger mitochondria into smaller elements(Friedman & Nunnari, 2014, Kageyama, Zhang et al., 2011). The effects of Drp1 driven mitochondrial fission is opposed by fusion between mitochondria driven by the Mitofusins and Opa1(Chen & Chan, 2017)(Schrepfer & Scorrano, 2016). Therefore, Drp1 repression allows unopposed mitochondrial fusion to sustain a hyperfused mitochondrial state. The other extreme state, i.e. unopposed mitochondrial fission, is critical for achieving pluripotency of stem cells during reprogramming (Prieto, Leon et al., 2016). However, sustained mitochondrial fission reduces pluripotency of stem cells (Zhong, Cui et al., 2019). Thus, a balance of timely fission and fusion of mitochondria appears to be critical for maintaining stem cell properties.

Enhanced mitochondrial fusion sustains stemness of certain adult stem cells of neural, germ line and mammary lineages (Khacho, Clark et al., 2016, Senos Demarco, Uyemura et al., 2019, Wu, Chen et al., 2019). Particularly, repression of Drp1 supports stemness and repression of Mitofusin or Opa1 inactivates stemness in adult mouse neural lineage (Iwata, Casimir et al., 2020, Khacho & Slack, 2017). In various tumors, the bulk tumor cell populations are maintained by the adult neoplastic stem cells (also called tumor initiating cells) as they self-renew, proliferate and differentiate (Magee, Piskounova et al., 2012). Drp1 has been linked to tumor formation in various cancer types (Nagdas, Kashatus et al., 2019, Serasinghe, Wieder et al., 2015, Tanwar, Parker et al., 2016, Tsuyoshi, Orisaka et al., 2020, Xie, Wu et al., 2015). Drp1 activation sustains neoplastic stem cells at least in the astrocytic lineage (Xie et al., 2015). Although various mechanisms and pathways have been proposed towards modulation

of stem cell properties by mitochondrial fission and fusion regulators, no common theme has yet emerged.

Given that stem cells exhibit plasticity at various levels, a detailed understanding of various states of these cells is an important area of investigation (Magee, Piskounova et al., 2012)(Folmes, Dzeja et al., 2012). We found that select neoplastic ovarian epithelial stem cells (marked by Aldh) have lower levels of mitochondrial fission and can convert to a state of elevated mitochondrial fission when self-renewal and proliferation is activated (Spurlock et al., 2019)(Spurlock et al., 2021b). Importantly, the cells with minimum mitochondrial fission were found within a neoplastic stem cell sub-population that has >10 folds self-renewal and proliferation ability compared to the other neoplastic stem cell subpopulation (Spurlock et al., 2019)(Spurlock et al., 2021b). Thus, we proposed, that a repressed mitochondrial fission state may prime neoplastic stem cells towards maximizing their potential of self-renewal and proliferation. Similar priming was demonstrated in a normal hematopoietic stem cell subpopulation that maintains Drp1 repression (Liang, Arif et al., 2020). However, the causative role of Drp1 in mitochondria driven priming of stem cell self-renewal/proliferation remains to be investigated. Nonetheless, an elevated mitochondrial fusion state, sustained by mitofusin, was shown to drive immortalization of neoplastic stem cells to support tumorigenesis in a Drosophila model (Bonnay, Veloso et al., 2020). Therefore, it is important to study the detailed involvement of mitochondrial fission and fusion in the mitochondria based priming of stem cell self-renewal and proliferation.

Here, we investigated involvement of Drp1 in mitochondria based priming of stemness during neoplastic transformation of skin cells. Skin stem cells sustain the regenerative capacity of the organ and thus serve as an excellent model for adult stem cells (Fuchs, 2016), while the role of Drp1 remains largely unknown in this system. Therefore, we took the first step of detailed investigation of the spontaneously immortalized skin keratinocyte cell line, HaCaT, which has been widely used to model the basic organization of skin and how carcinogens impact it (Boelsma, Verhoeven et al., 1999, Jung, Jung et al., 2016, Schoop, Mirancea et al., 1999). The HaCaT cells carry a non-functional p53 (St John, Sauter et al., 2000), which provides the appropriate cellular context given Drp1 inactivation increases cell proliferation in the absence of

active p53 (Mitra, Rikhy et al., 2012, Mitra, Wunder et al., 2009). Here, we tested if Drp1 repression is involved in mitochondria based priming of stem cells towards driving neoplastic transformation.

RESULTS AND DISCUSSION

Keratinocytes transformed under mild carcinogenic stress exhibit attenuated Drp1 activity and have abundant self-renewing/proliferating cells

The potent carcinogenic impact of the chemical carcinogen 2,3,7,8-tetrachlorodibenzodioxin (TCDD), an environmental pollutant, has been widely studied on the HaCaT line as well as on skin tissue (Wincent, Bengtsson et al., 2012)(Hao, Lee et al., 2012)(Ray & Swanson, 2004)(Mulero-Navarro & Fernandez-Salguero, 2016)(Der Vartanian, Quetin et al., 2019). We used both mild and strong dose of TCDD to uncover any possibility of mitochondria based stemness priming during TCDD driven neoplastic transformation. TCDD driven carcinogenesis is largely caused by activation and upregulation of the aryl hydrocarbon receptor (AHR) (Mulero-Navarro & Fernandez-Salguero, 2016) (Leclerc, Staats Pires et al., 2021). Exposure to milder (T-1nM) and stronger (T-10nM) doses of TCDD causes a comparable increase in cell proliferation of HaCaT cells within 3 weeks of standard TCCD driven transformation protocol, with Toluene used as the vehicle control (Fig. 1A). The stable transformed colonies of TCDD-1nM (TF-1) and TCDD-10nM (TF-10) maintain comparable upregulation of AHR, even in the absence of TCDD (Fig. 1B). Unlike the parental HaCaT cells (Parental), both transformed cells are able to form subcutaneous xenograft tumors, confirming their transformation status (Extended. Fig. 1A). Interestingly, pathological evaluation of H&E stained tumor sections revealed that the TF-1 cells gave rise to malignant tumors harboring less differentiated (primitive) squamous cells with large nuclei (blue) and little visible cytoplasm (pink) (Fig. 1C, left). Whereas the TF-10 cells formed tumors harboring differentiated stratified squamous epithelium with cells having expansion of cytoplasm (Fig. 1C, right); the clear gaps represent artifacts secondary to cryo-sectioning.

Given the above differences between the TF-1 and TF-10 populations, we probed for any difference in Drp1 and mitochondrial shape, as well as self-renewal and proliferation abilities between them and the non-transformed Parental population. Among the major molecules regulating mitochondrial fission and fusion (Drp1, Mfn1, Mfn2, Opa1), Drp1 exhibited the most prominent differences (Fig. 1D). Particularly, the TF1 population has markedly lower levels of the cell cycle regulated activating phosphorylation of Drp1 (pDrp1-S616), while both the transformed populations have higher levels of Drp1 protein compared to the Parental line (Fig. 1D). The TF-1 population also has lower levels of other tested mitochondrial markers (Tom20, Cytochrome C and Fis1), compared to the TF-10 population (Extended Fig. 1B). Next, to assess the steady state contribution of mitochondrial fission and fusion on mitochondrial shape we quantified mitochondrial [Fission] and [Fusion5] metrics in individual live cells stably expressing the fluorescent mitochondrial reporter, mitoPSmO (Spurlock et al., 2019)(Spurlock et al., 2021b) (Fig. 1E). In comparison to the TF-1 and Parental populations, the TF-10 population exhibits reduced levels of the [Fusion5] metric and slightly elevated level of the [Fission] metric (Fig. 1F). Notably, although the TF-1 population has higher median [Fusion5], lower range of [Fusion5] is also detected in this population (Fig. 1F). Since the [Fusion5] metric reflects mitochondrial length in each cell (Spurlock et al., 2019), this data suggests a wider range of mitochondrial length in the TF-1 population, which could be potentially brought about by regulating Drp1 driven mitochondrial fission (Fig. 1D).

Drp1 repression brings about a p53 dependent cell cycle block (Mitra et al., 2009), and can increase cell proliferation in the absence of functional p53 (Parker, Iyer et al., 2015)(Mitra et al., 2012). Consistent with this, the TF-1 HaCaT population with inactive p53 status (St John et al., 2000) and low levels of active Drp1 (Fig. 1D) have significantly higher *in vitro* cell proliferation rate, compared to the Parental and the TF-10 population (Fig 1G). Furthermore, the TF-1 population form markedly larger spheroids in conditions that support self-renewal and proliferation, in comparison to those formed by the Parental or the TF-10 population (Fig. 1H). More importantly, ELDA statistics applied on spheroid formation assay for determination of *in vitro* stem cell frequency (Hu & Smyth, 2009) demonstrated that the TF-1 population has double the

abundance of self-renewing/proliferating cells than the TF-10 population, while their abundance is one order higher in both transformed populations compared to the Parental (Fig. 1I).

In summary, the above data demonstrate that keratinocytes transformed with low dose of the potent carcinogen, TCDD, maintain attenuated Drp1 activity ([Drp1]-att), greater self-renewal/proliferative ability and form less differentiated tumors compared to those transformed by a 10-fold higher TCDD dose. Thus, we conclude that the [Drp1]-att TF-1 keratinocyte population is enriched in neoplastic stem/progenitor cells.

Drp1 attenuated TF-1 keratinocyte population maintains an expanded slow-cycling sub-population with elevated stem/progenitor cell markers

Single cell methods, particularly single-cell-RNAseq (scRNA-seq), are widely used to identify and characterize distinct cellular states in a given cell population (Luecken & Theis, 2019). To identify and define the neoplastic stem cells of the Drp1 attenuated TF-1 population, we performed scRNA-seq of the Parental and the transformed populations. Cell clustering in a UMAP plot shows 6 clusters within Parental, TF-1 and TF-10 populations (Fig. 2A, Clusters 0-5). While Cluster 4 is reduced in both transformed populations in comparison to the Parental, the TF-1 population exhibits a marked expansion of Cluster 3 and reduction of Cluster 5 (Fig. 2A, Extended. Fig.2A, left panel). These results also hold true with the lowest cluster resolution (Extended. Fig. 2B. arrows). Heat map of cluster markers altered by at least 1.5 folds (p-adjusted <0.0001) shows that Clusters 2,3 and 4 are marked by upregulation of distinct genes while Cluster 5 is marked by overall downregulation of various genes (Extended Fig. 2C, Extended. Data Table 1). From here, we identified the top most candidate genes to mark each cluster (color coded arrows in Extended Fig. 2C). Indeed, the neoplastic stem/progenitor cell enriched Drp1-att TF-1 population shows >3-fold upregulation of the epidermal stem cell marker Krt15 (Giroux, Lento et al., 2017, Gonzales & Fuchs, 2017, Purba, Haslam et al., 2014) and of the neoplastic stem cell markers for skin carcinomas, SOX2 and SOX4 (Boumahdi, Driessens et al., 2014, Foronda, Martinez et al., 2014) (Fig. 2B, arrow). Since the markers increase across all TF-1 clusters, with maximum levels in Cluster 3, we conclude that the TF-1 population

exhibits upregulation of the stem/progenitor markers independent of their cluster distribution. On the other hand, the other stem/progenitor cell markers, like Krt5, Krt14, Krt19 (Gonzales & Fuchs, 2017)(Karantza, 2011) are also enriched by ~2-fold in Cluster 3, but comparably in all the three cell populations, as exemplified by Krt5 (Fig. 2B, arrow, Extended Data Table 1). Notably, among the 3 cell populations, TF-1 harbors markedly fewer cells in Cluster 3 having elevated levels of the differentiating cell marker Krt13 (Karantza, 2011). Cluster 5, reduced in TF-1 population, is marked by 1.5 to >2-fold reduced expression of 12 of the 13mtDNA genes in all the 3 cell populations (Extended Fig. 2D, arrow). Cluster 4, reduced in both transformed populations, is marked by >8-fold upregulation of OASL, a gene involved in the interferon pathway, in all the three cell populations (Extended Fig. 2E).

Since flow cytometry on PI stained cells revealed modest differences in cell cycle distribution between the Parental and transformed populations (Extended. Fig. 2A, right panel), we asked if the scRNA-seq derived clusters represent distinct cell cycle phases. Therefore, we performed the standard gene set enrichment analyses (GSEA) of the overall cluster marker profiles using the REACTOME pathway database (Subramanian, Tamayo et al., 2005) (Extended. Data Table 2). Some of the statistically significant pathways (q value <0.01) were renamed based on the leading-edge genes of the identified pathways. GSEA showed upregulation of genes in “Mitosis and Relevant Cytoskeletal Proteins” in Cluster 2 and that of genes in “DNA repair / replication and Histones” in Cluster 0 (Fig. 2C); Cluster 1 has downregulation of “Histones and Ubiquitin related” genes. Indeed, the mitotic Cyclin B and its partner kinase CDK1, as well as Cyclin A are markedly higher in Cluster 2-G2-M, while PCNA, which peaks early in S phase (Maga & Hubscher, 2003, Zerjatke, Gak et al., 2017) is highest in Cluster 0-S-Histone-hi in all 3 cell populations (Fig. 2D); the S phase cyclins E1/E2 and their partner CDK2 were not detected in our sc-RNAseq data set. Surprisingly, Cluster 3 (positively marked by Krt15) has dramatic downregulation of genes in “Overall Cell Cycle” as well as the above categories representing distinct cell cycle phases (Fig. 2C), suggesting their cell cycling is slow. This is reflected in dramatic low levels of cyclins in Cluster 3-SloCycl-Krt15-hi in all three cell populations, most prominently in TF-1 (Fig. 2D). More importantly, the levels of PCNA, whose transcripts are dramatically reduced in

quiescent cells (Maga & Hubscher, 2003, Zerjatke, Gak et al., 2017), is markedly reduced in the SloCycl-Krt15-hi cluster (and others) only in the TF-1 population (Fig. 2D). This cluster indeed has upregulation of genes involved in “Keratin” and “Signaling” pathways. Notably, the Notch pathway target, Hes1, which actively maintains quiescence (Sang, Coller et al., 2008) (Moriyama, Durham et al., 2008), is upregulated across the clusters in the TF-1 population (Extended Fig. 2E). These data strongly suggest that the enrichment of the SloCycl-Krt15-hi cluster in the TF-1 population happens due to active maintenance of quiescence, rendering them slow cycling. Cluster 4 does not relate to cell cycle and shows upregulation of genes related to “Cytokine” (interferons) pathway (Fig. 2C), many of which are suppressed by AHR activation (Di Meglio, Duarte et al., 2014) (Extended. Data Table 1). Thus, comparable upregulation of AHR in both transformed populations (Fig. 1B) could explain their comparable reduction of Cluster 4 (Fig. 2A). The downregulated mtDNA genes in Cluster 5 were identified as “TCA cycle” and “Complex 1 biogenesis” in our overrepresentation analyses (* in Fig. 2C), but not in GSEA. Towards understanding the entry into the slow cycling state of the Krt15hi-Cluster 3, we performed trajectory analyses using Slingshot algorithm that identifies clusters related to each other based on their gene expression (Street *et al*, 2018). The output trajectory was the following: “G2-M” to “S-Histones-hi” to “Cytokine” to “Histones/Ub-lo” bifurcating into “SloCycl-Krt15-hi” or “mtDNA-lo” (Fig. 2C, open arrows, Extended. Fig. 2F). This implies that the cells in the TF-1 population may preferentially reside in the SloCycl-Krt15-hi cluster and not in the mtDNA-lo cluster, thus expanding the former and reducing the latter (Fig. 2A).

Given the above striking differences in cell cycle genes between the clusters, we quantified cell cycle distribution in each cluster in the Parental, TF-1 and TF-10 populations. We used a Seurat algorithm that employs several validated predictive cell cycle genes to quantify G2-M and S scores, and assign cells in G2-M, S or in G1/G0 (when both G2-M and S phase scores are low) (Tirosh *et al*, 2016). We found that the G2-M score is overall comparable between Parental and the transformed populations, while the TF-1 population has lower S score (Fig. 2E). Distribution of cell cycle phase across the clusters indeed corroborated the major conclusions from GSEA, namely Cluster 2 is abundant in G2-M cells, Cluster 0 (and 1) in S and Krt15 marked Cluster 3

is in G0/G1 (expected for quiescent/slow-cycling cells) (Fig. 2F,G). This data, taken with the lower levels of Histone transcripts in Cluster 1 than in Cluster 0 (* in Fig. Extended 2C) suggest that Cluster 0 is early S phase while Cluster 1 is late S phase. While the G2-M and S cells are equally abundant in all three cell populations, the expanded SloCycl-Krt15-hi cluster in the TF-1 population has significantly more cells in G0/G1 and less cells in S than the other two populations (Fig. 2F,G, arrows). On the other hand, the reduced mt-DNA-lo cluster in the TF-1 population has more cells in S and less in G0/G1 population (Fig. 2F,G, arrows). Quantification of this reciprocal relationship of G1 and S distribution between Cluster 3 and 5 revealed that the G1 to S reciprocity between Cluster 3 and 5 is >5-fold in the TF-1 population with respect to the Parental and TF-10 population (Fig. 2G, inset). This suggests that altered cell cycle regulation in the TF-1 population may allow them to preferentially reside in the 3-SloCycl-Krt15-hi cluster and not in the 5-mtDNA-lo cluster. Such a regulation may involve attenuation of CDK1 driven Drp1(S616) phosphorylation (Fig. 1D) due to marked reduction of CyclinB/CDK1 particularly in the TF-1 population in late S phase (Fig. 2D), where decision for expansion of the slow cycling Krt15-hi cluster is likely made (Fig. 2C, Suppl Fig. 2F).

In summary, our sc-RNAseq data demonstrate that the [Drp1]-att TF-1 keratinocyte population enriched with self-renewing cells maintain an expansion of slow cycling cells expressing high levels of stem/progenitor markers Krt15 (lineage specific) and Sox2 and Sox4 (general), likely due to altered cell cycle regulation. Consistent with our data, the Krt15+ epidermal stem cells are primarily slow cycling and when activated give rise to various epithelial cell types or contribute to epidermal carcinoma development (Giroux et al., 2017, Gonzales & Fuchs, 2017, Purba et al., 2014)(Morris, Liu et al., 2004)(Giroux et al., 2017). Moreover, the higher *in vitro* cell proliferation rate of the [Drp1]-att TF-1 keratinocytes (Fig. 1G) could result from the higher clonogenic capacity of the Krt15-hi cells (Morris et al., 2004)(Seykora & Cotsarelis, 2011).

Fine-tuned repression of Drp1 sustains a [CyclinE^{hi}-Sox2^{hi}-Krt15^{hi}] state and accelerates carcinogen driven cell transformation

Repression of Drp1 driven mitochondrial fission elevates stem/progenitor cell markers in mouse embryonic fibroblasts, and in cells of neural and ovarian epithelial

lineage (Iwata et al., 2020, Parker et al., 2015). In the epidermal lineage, Krt15+ self-renewing stem cells contribute to both skin regeneration and carcinoma development (Giroux et al., 2017, Gonzales & Fuchs, 2017, Purba et al., 2014), while Sox2 upregulation in neoplastic stem/progenitor cells particularly supports skin carcinoma (Boumahdi et al., 2014, Siegle, Basin et al., 2014). We found that, in comparison to the Parental and TF-10 keratinocyte populations, Sox2 protein levels are dramatically higher in the Drp1 attenuated TF-1 population (Fig. 3A, Extended Fig. 3A), which are enriched for self-renewing cells, have higher in vitro cell proliferation rate and forms less differentiated tumors (Fig. 1). This also corroborates the elevated Sox2 transcript level seen across the scRNA-seq derived clusters in the TF-1 population (Fig. 2B). Krt15 protein levels are elevated in both transformed populations in comparison to the Parental (Fig. 3A), unlike the cluster specific differences in transcript levels (Fig. 2B). We did not detect any increase in other embryonic stem cell markers like Oct4 or Nanog in the TF-1 population (Extended Fig. 3A). Immunostaining based co-expression analyses of Sox2 and Krt15 in individual cells revealed that only a subpopulation of Drp1 attenuated TF-1 population has elevation of both Krt15 and Sox2 (Fig. 3B, Extended. Fig. 3B). Similar analyses showed that the highest levels of Sox2 in the TF-1 population is sustained in cells with an intermediate level of Drp1 protein levels (Fig. 3C) and lower pDrp1(S616) levels (indicative of lower Drp1 activity) (Fig. 3D). Therefore, we investigated whether repression of Drp1 in the Parental cells may cause the elevation of Sox2 and/or Krt15 observed in the TF-1 population derived from the Parental cells (with carcinogen treatment). To that end, we knocked down Drp1 expression in Parental keratinocytes with two validated Drp1 shRNAs (Parker et al., 2015, Tanwar et al., 2016), one weaker (W), and the other with 5 folds stronger Drp1 knockdown efficacy (S) almost mimicking Drp1 genetic ablation (Fig. 3E). Surprisingly, while weaker Drp1 knockdown elevates Krt15 levels, while the stronger Drp1 knockdown fails to do so (Fig. 3E). On the other hand, both weak and strong Drp1 knockdown caused marked elevation of Sox2 in a graded fashion (Fig. 3E). The increase in Sox2 with Drp1 repression in the keratinocytes is consistent with findings in Drp1 ablated mouse embryonic fibroblasts (Parker et al., 2015) and neural stem cells (Iwata et al., 2020). Thus, unlike the stronger Drp1 knockdown, the weaker Drp1 knockdown maintains detectable Drp1 protein, and

uniquely sustains a Sox2-hi/Krt15-hi population characteristic of the naturally Drp1 attenuated TF-1 population.

Cell cycle status is a crucial determinant of stemness (Orford & Scadden, 2008, Otsuki & Brand, 2018, Pauklin & Vallier, 2013). Sox2 expression is under the influence of various G1 cyclins (Liu, Michowski et al., 2019). Cyclin E, which is indispensable for S phase entry from quiescence and also for neoplastic transformation (Geng, Yu et al., 2003, Siu, Rosner et al., 2012), is critical for sustaining Sox2 expression (Liu et al., 2019). Interestingly, among the major cyclins, Cyclin E1 levels are particularly higher in the Sox2 enriched Drp1 attenuated TF-1 population, when compared to the Parental, while Cyclin D is particularly higher in the TF-10 population (corroborating sc-RNAseq data, Fig. 2D) (Fig. 3F). Moreover, Cyclin E1 is preferentially accumulated in the nucleus in the TF-1 population, which is required to impact gene expression of Sox2 (and others) (Fig. 3G,H). Stringent regulation the Cyclin E protein levels involves its degradation triggered by phosphorylation by its cognate kinase CDK2 at the T62 residue (Siu et al., 2012). Thus, level of pCyclinE(T-62) reflects the level of active Cyclin E that drives transcription and remains susceptible to degradation. Immunostaining based co-expression analyses showed that in the TF-1 population, elevated Sox2 is sustained in cells with lower level of pCyclinE(T-62) than in the Parental population that has overall lower levels of Sox2 (Fig. 3I). Moreover, cycloheximide chase assay, to assess degradation rate of proteins, revealed no Cyclin E degradation in TF-1 cells in comparison to marked CycE degradation in the Parental cells; both populations maintain Tom20 (mitochondrial marker) within the 2 hour assay time frame (Extended. Fig. 3C). Thus, our data is consistent with elevated Sox2 in the TF-1 population being sustained by elevated Cyclin E levels achieved by attenuation of its degradation kinetics. Given, mitochondrial regulation of Cyclin E regulates Cyclin E degradation (Mandal, Freije et al., 2010, Parker et al., 2015), we tested if repression of Drp1 driven mitochondrial fission in the Parental cells can elevate Cyclin E levels towards sustaining the observed elevated Sox2 levels. Indeed, Cyclin E is dramatically accumulated in the nucleus in a graded manner with Drp1 knockdown efficacy (Fig. 3J,K), similar to Sox2 (Fig. 3E). Thus, our data shows that Drp1 repression elevates nuclear Cyclin E and Sox2 levels, which is characteristic of the naturally Drp1 attenuated TF-1 population.

Given, Sox2 and Cyclin E are important for neoplastic transformation in various cancer types (Hwang & Clurman, 2005, Schaefer & Lengerke, 2020, Teixeira & Reed, 2017), and Krt15+ cells give rise to skin carcinoma (Li, Park et al., 2013, Seykora & Cotsarelis, 2011), we asked if repression of Drp1 can modulate the process of carcinogen driven neoplastic transformation of keratinocytes. Thus, we exposed control and Drp1 knockdown Parental keratinocytes to 1 and 10nM TCDD following standard TCDD driven transformation protocol. Interestingly, the weaker Drp1 knockdown, which maintains Krt15-hi/Sox2-hi status and elevated nuclear Cyclin E, got transformed by 10nM TCDD even earlier than the control (Fig. 3L); 1 nM TCDD did not cause any transformation at this time point. This happened in spite of their lower proliferation rate than the control in the earlier time point. On the other hand, the stronger Drp1 knockdown, which also maintained slower cell proliferation rate and a Krt15-lo/Sox2-hi status with elevated nuclear Cyclin E, is not transformed in the same time window (Fig. 3L).

In summary, our data suggest that fine-tuned repression (ftr) of Drp1, sustained by incomplete knockdown of Drp1, allows enrichment of a [$Drp1^{ftr}$-$CyclinE^{hi}$-$Sox2^{hi}$-$Krt15^{hi}$] state that is particularly susceptible to neoplastic transformation by higher TCDD dose. This primed state is characteristic of the neoplastic stem/progenitor cell enriched [$Drp1^{att}$-$CyclinE^{hi}$-$Sox2^{hi}$-$Krt15^{hi}$] TF-1 population resulting with lower TCDD dose. Moreover, close to complete repression of Drp1 sustains a [$Drp1^{lo}$-$CyclinE^{hi}$-$Sox2^{hi}$-$Krt15^{lo}$] state, and does not support transformation as reported for Drp1 ablated MEFs (Serasinghe et al., 2015).

Fine-tuned repression of Drp1 maintains smaller fused mitochondrial elements, and sustains transcriptomic profile similar to the neoplastic stem cell enriched TF-1 population

Towards understanding the mechanism of fine-tuned (incomplete) Drp1 repression driven priming of neoplastic transformation, we performed detailed comparison of mitochondrial shape and over all gene expression between the Parental keratinocytes expressing control, weak or strong Drp1 shRNAs. Quantification of mitochondrial fission and fusion metrics contributing to mitochondrial shape in live cells

confirmed that the stronger (more complete) Drp1 knockdown maintains ~77% of the cells in the hyperfused state i.e. [Fission] metric <0.2 and [Fusion5] metric >80 (Spurlock et al., 2019), while the control population maintains ~55% of the cells in this state (Fig. 4A, blue box, Extended. Fig. 3D). On the other hand, the weaker (incomplete) Drp1 knockdown maintains only ~40% of the cells in the hyperfused state (Fig. 4A, blue box), while uniquely maintaining ~28% of the cells in the [Fission] range of 0.2-0.4 and [Fusion5] range of 40-80 (Fig. 4A, red box). Closer examination of cells within this unique population in the weaker Drp1 knockdown population revealed distinct mitochondrial fragments along with extensive tubular mitochondria, as opposed to uniformly hyperfused mitochondria (Extended Fig. 3D). To understand this distribution better, we probed the relationship of mitochondrial fission and fusion metrics with the mitochondrial number and length metrics that they are derived from. The cells with the unique mitochondrial fission/fusion state (Fission: 0.2-0.4 and Fusion5: 40-80) have lower mitochondrial number and total mitochondrial length (Fig. 4B), signifying decrease in mitochondrial content in this subpopulation. However, cells with hyperfused mitochondria (Fission<0.2; Fusion5>80) have distinctly higher mitochondrial number in the weaker Drp1 knockdown population but have comparable mitochondrial length to those in the stronger Drp1 knockdown population (Fig. 4B). To confirm that such an increase in mitochondrial number in the weaker Drp1 knockdown with hyperfused mitochondria is due to a greater number of smaller mitochondrial hyperfused networks, we quantified the percent length of the longest mitochondrial elements (Fusion1). Indeed, less than 7% of cells have >80% of the mitochondrial length as hyperfused in the weaker Drp1 knockdown, compared to ~40% in the stronger Drp1 knockdown (Fig. 4C, top). More importantly, the enriched population of cells in the weaker Drp1 knockdown with fission range of 0.2-0.4 have only up to 40% of the mitochondrial lengths in fused networks (Fig. 4C, bottom). We detected cells with similar mitochondrial fission and fusion features particularly in (FACS sorted) mitochondria primed ovarian neoplastic stem cell population that has 10-fold higher ability of self-renewal and proliferation (Spurlock et al., 2021b). Therefore, these data demonstrate that the fine-tuned Drp1 repression, which primes cells for transformation, enriches a subpopulation of cells maintaining more number of smaller fused mitochondrial

elements, distinct mitochondrial puncta and minimal mitochondrial content (Extended Fig. 3D). We conclude that the remnant Drp1 driven mitochondrial fission in the weaker Drp1 knockdown population prevents the net fusion of the smaller fused elements to form a larger hyperfused mitochondrial network, and may also underlie generation of the mitochondrial puncta. We speculate that the functional significance of such previously unappreciated distinctions in mitochondrial shape may involve Drp1 driven regulation of mitophagy (Twig & Shirihai, 2011).

To probe the contribution of gene expression of any particular cell population in neoplastic transformation after Drp1 repression, we performed sc-RNAseq of the control and Drp1 knockdown Parental populations. First, we compared the overall gene expression within the gene coverage in our scRNA-seq data set. Indeed, the weaker Drp1 knockdown, which maintains higher Drp1 transcript levels, modulates a smaller gene set to a smaller degree compared to the stronger Drp1 knockdown that maintains lower Drp1 transcript levels (Extended. Fig. 4A, B). However, graded Drp1 knockdown has both ‘similar’ (graded upregulation or downregulation) and ‘opposite’ effects (upregulation in one and downregulation in the other) (Extended Fig. 4C). The opposite effect is dominated by Krt15, Krt13, Krt4, Krt5 transcripts being upregulated in the weaker Drp1 knockdown and downregulated in the stronger Drp1 knockdown (color coded * in Fig. 4D, Extended Fig. 4C), corroborating our findings on Krt15 protein levels (Fig. 3E). On the other hand, genes for various mitochondrial proteins, involved in mitochondrial energetics, redox or biogenesis, were upregulated particularly in the stronger Drp1 knockdown (Fig. 4E upper panel, Extended Fig. 4C, bold). This is consistent with our observation of decreased mitochondrial content in the weaker Drp1 knockdown (Fig. 4B). Synthesis of the mitochondrial proteins can be potentially sustained by elevated ribosomal genes and genes involved in protein synthesis in the stronger Drp1 knockdown (Fig. 4E, lower panel). Although Drp1 repression has been linked with regulation of ribosomal genes and protein synthesis (Tanwar et al., 2016)(Zhao Q et al., 2021)(Favaro, Romanello et al., 2019), this area warrants further focused investigation.

Next, we performed cell clustering in a UMAP plot and obtained 6 clusters (Extended. Fig. 4D, Extended Data Table 3). Based on the remarkable correspondence

of the top conserved cluster markers identified in the Parental/transformed data set (Fig.2), we assigned cluster identities of G2-M, S-early, S-late, mtDNA-lo, SloCycl-Krt15-hi and Cytokine to the control and Drp1 knockdown data set (Extended. Fig. 4D). The number of common cluster markers show overall 40-80% correspondence between the two data sets, with some exceptions in the S-late and mtDNA-lo clusters (Extended. Fig. 4E). Strikingly, the weaker Drp1-knockdown population exhibits expansion of the SloCycl-Krt15-hi cluster and reduction of the Cytokine and mtDNA-lo clusters observed in the [Drp1^{att}-CyclinE^{hi}-Sox2^{hi}-Krt15^{hi}] TF-1 population, albeit to a lesser degree (Fig. 4F). This similarity in cluster organization suggests that the non-transformed Parental population with fine-tuned Drp1 repression establishes a gene expression profile to poise the cells for neoplastic transformation, and thus explains their accelerated neoplastic transformation ability only with higher TCCD dose (Fig. 3L). On the other hand, the stronger Drp1 knockdown markedly reduced the abundance of the SloCycl-Krt15-hi cluster and exhibits overall opposite trend of cluster profile compared to the weaker Drp1 knockdown and TF-1 population (Fig. 4F). Krt15 and various other marker Keratin genes are dramatically suppressed across the clusters in the stronger Drp1 knockdown and while they are over all elevated in the weaker Drp1 knockdown (Extended Fig. 4F). This data, suggesting that impact of the level of Drp1 repression on specific keratin transcripts is direct and not due to cluster organization, confirms and expands our findings on Krt15 protein levels (Fig. 3E). Moreover, analyses of cell cycle distribution (as in Fig. 2) revealed higher G2-M score and less S score in the stronger Drp1 knockdown, while weaker Drp1 knockdown has similar cell cycle distribution to the control (Fig. 4G). The stronger Drp1 knockdown maintains more cells in G2-M and less cells in S particularly in the SloCycl-Krt15-hi as well as the mt-DNA-lo cluster (Extended. Fig. 4H), contradictory to their reciprocal nature in the TF-1 population (Fig. 2). The dramatic reduction of the SloCycl-Krt15-hi cluster in the stronger Drp1 knockdown cells could be due to their inability of exiting the elevated CyclinB1/CDK1 driven G2-M regulation in this cluster (Fig. 4H, left). Also, the stronger Drp1 knockdown maintained marked elevation of the growth factor cyclin, Cyclin D2 and reduction of the S phase marker, PCNA, across clusters (Fig. 4H, right); Cyclin E1 and Sox2 transcripts were not detected in this data set. Therefore, our data shows that fine-tuned repression of Drp1,

which accelerates carcinogen induced cell transformation, maintains a gene expression profile characteristic of the [Drp1^{att}-CyclinE^{hi}-Sox2^{hi}-Krt15^{hi}] TF-1 population. The stronger Drp1 knockdown fails to do so, has cell cycle disturbances and dramatically reduced expression of relevant keratin genes. We speculate that repression of Drp1 beyond an optimal level may initiate compensatory changes through the retrograde pathway to trigger mitochondrial biogenesis and suppress relevant keratin genes (Ryan & Hoogenraad, 2007).

Taken together, our detailed molecular analyses of the *in vitro* keratinocyte model suggest that a "goldilocks" level of fine-tuned repression of Drp1 accelerates neoplastic transformation by priming a distinct stem/progenitor-like state (Fig. 5). We propose that the priming is brought about by flexibility of Drp1 regulation that sustains distinct mitochondrial and gene expression characteristics leading to the enrichment of a slow cycling [Drp1^{ftr}-CyclinE^{hi}-Sox2^{hi}-Krt15^{hi}] stem/progenitor-like state. Cyclin E, which maintains expression of stem cell markers, is indispensable for exiting cell cycle quiescence and also for neoplastic transformation (Hwang & Clurman, 2005, Schaefer & Lengerke, 2020, Teixeira & Reed, 2017) (Liu et al., 2019). We speculate that the slow cycling [Drp1^{ftr}-CyclinE^{hi}-Sox2^{hi}-Krt15^{hi}] stem/progenitor-like state has reduced depth of cell cycle quiescence (van Velthoven & Rando, 2019) towards rapidly transitioning to a self-renewing/proliferation state to support neoplastic transformation. Such transition may involve further activation of mitochondrial fission induced by signaling pathways supporting stemness, which would be prevented with supra-optimal Drp1 knockdown (as shown here) or total ablation of Drp1 (as reported) (Kashatus, Nascimento et al., 2015, Serasinghe et al., 2015, Spurlock et al., 2019). This conceptualization helps explain how regulated reduction and increase of Drp1 activity can potentially maintain adult stem cell properties (Iwata et al., 2020, Khacho & Slack, 2017, Parker et al., 2015, Xie et al., 2015). Furthermore, our data raises the possibility that the [Drp1^{att}-CyclinE^{hi}-Sox2^{hi}-Krt15^{hi}] TF-1 population represents an early stage of neoplastic transformation when stem cells self-renew to form less differentiated tumors, unlike the differentiated tumors formed by the [Drp1^{hi}-CyclinE^{lo}-Sox2^{lo}-Krt15^{hi}] TF-10 population. Further *in vivo* validation of our findings would reveal if and how bodily stresses causing mild repression of Drp1 driven mitochondrial fission, can possibly enrich the mitochondria

primed stem/progenitor-like population in tissues making them susceptible to neoplastic transformation. Enhanced mitochondrial fusion, proposed as a required event of neoplastic transformation of stem cells (Bonnay et al., 2020), may also involve such mitochondria driven priming.

MATERIALS AND METHODS

Materials

Biochemicals were obtained from Fisher Biochemicals or Sigma. Other materials: Drp1 shRNA (Dharmacon); Flouromount G (SouthernBiotech); FuGENE® 6 Transfection Reagent (Promega); Luminata Forte Western HRP substrate (Millipore); 4% paraformaldehyde aqueous solution and Triton X-100 (FisherScientific); Labtek chambers (Nalgene Nunc International); DMEM (GIBCO); Geltrex (GIBCO); Primary antibodies were against: Drp1 (western blotting, 1:1000; immunofluorescence, 1:100; BD Biosciences); Cyclin E1 (HE12) (western blotting, 1:1000; immunofluorescence 1:100; Cell Signaling); actin AB-5 (1:10000; BD Biociences), Sox2 (western blotting, 1:500; immunofluorescence, 1:100; BD Bioscience), HSP-60 (1:200; BD Bioscience); Cytokeratin 15 (western blotting, 1:2000; immunofluorescence, 1:200; Abcam); Oct4 (immunofluorescence, 1:50; Cell Signaling); Nanog (immunofluorescence, 1:50; Cell Signaling). Secondary antibodies were from Jackson ImmunoResearch Laboratories. Athymic nude mice were purchased from Jackson laboratories.

Cell culture methods

HaCaT cells were cultured on plastic dishes in Dulbecco's Modified Eagle's Medium (DMEM) with high glucose (4.5 g/L), sodium pyruvate (1 mM), L-Glutamine (4 mM), Penicillin (100 U/mL), Streptomycin (100 µg/mL), and 10% FBS using standard techniques. Transformed keratinocytes were derived from the Parental HaCaTs by selecting multiple clones after treatment with the noted dose of TCDD with replenishment with fresh TCDD every 2-3 days. The derived lines were treated with two courses of BM-Cyclin treatment to eliminate any mycoplasma infection.

Transfections were preformed using Fugene 6 Transfection Reagent modifying manufacturer's protocols. Lines stably expressing Drp1-shRNAs or PSmO were selected using puromycin treatment (2 µg/mL) with regular media changes for 2 weeks until resistant colonies grew. The stable Drp1 knockdown lines were treated with two courses of BM-Cyclin treatment to eliminate any mycoplasma infection.

Standard cell proliferation assay was performed as described in (Parker et al., 2015). The extreme limiting dilution analysis (ELDA) of spheroid formation ability was performed by seeding 1, 10, 100, and 1000 cells per well with 24 wells per dose in a 96 well UltraLow Attachment plate and TIC-supporting media (DMEM:F12 supplemented with human growth factors as published elsewhere (Spurlock et al., 2019)). Wells were Extendedemented with media equaling 10% of the total volume every second day. On Day 5, the total number of wells for each dose containing nascent spheroids was tabulated. The online ELDA tool was used to analyze the results (Hu & Smyth, 2009).

Immunoblotting and Immunofluorescence

Immunoblotting was performed using standard techniques. Whole cell lysates were run on 10% polyacrylamide gels and transferred to PVDF membranes followed by probing with appropriate primary and secondary antibodies.

Immunofluorecence was performed as described previously (Parker et al., 2015) on cells seeded in LabTek 8-well glass bottom or slide chambers. Briefly, cells were fixed in freshly prepared 4% aqueous paraformaldehyde supplemented with 4 %w/v sucrose and permeablized in freshly prepared 0.1 % Triton X-100 prior to staining. Immunostained cells were mounted in Fluoromount with DNA stain Hoechst 33342 (10 µg/mL).

Confocal microscopy, image processing and analysis

Confocal microscopy was performed on a Zeiss LSM700 microscope equipped with 405 nm, 488 nm, 555 nm, and 639 nm lasers, using the proprietary Zen Black (2012) software. Confocal micrographs were acquired with optimized laser powers and appropriate filters to minimize crosstalk, cross-excitation and bleaching. Live cells were imaged using a temperature and CO_2 controlled chamber set to 37 C and 5% CO_2.

Image processing and analysis of relative protein abundance and localization were performed using Zen Black and Zen Blue software to obtain background corrected mean fluorescence intensities within defined regions of interest drawn on maximum intensity z-projections of optical slices. Nuclear and cytosolic regions were demarcated based on DNA stain Hoechst 33342 and the immunostain of the molecule of interest, respectively. The [Fission] and [Fusion1/5] metrics using MitoGraph v2.1 software run on 3D stacks of confocal optical slices acquired from live cells expressing mito-PSmO or stained with Mitotracker Green, as described in (Spurlock et al., 2019). [Fission] is total mitochondria number / total mitochondrial length; [Fusion5] is (sum of top 5 mitochondrial length / total mitochondrial length) X 100. Microsoft Excel and IBM SPSS Statistics 23 were used to perform background corrections, bivariate analyses and significance testing.

Tumor Forming Assay in mice and histochemistry

5 million transformed HaCaT cells were injected in subcutaneously in the flank of athymic nude mice to form xenograft tumors. Prior to injection, cells were trypsinized and washed once with sterile PBS, and finally resuspended to 25,000 cells/μL in room temperature PBS with Geltrex. Tumors arising within 6 to 8 months were harvested for histochemical analyses. The harvested tumors were frozen unfixed in TissueTek OCT compound on dry-ice. A Cryostat was used to obtain 5 μm slices, which were then fixed using freshly made cold 4% paraformaldehyde and then stained with H&E using standard techniques.

Single Cell RNAseq and data analyses

Trypsinized single cells were washed in PBS (without ca++ or Mg++) with 0.04% BSA and tested for >90% viability. Single cell analysis was performed on a 10xGenomics platform according to 3' v3.1 NextGem Dual Index manual. The 3'-biased cDNA libraries were constructed through the following steps: cDNA fragmentation, end repair & A-tailing, and size selection by SPRIselect beads, adaptor ligation, and sample index PCR amplification, and then SPRIselect beads size selection again. The final constructed 3'-biased single cell libraries were sequenced by Illumina Nextseq500 machine, targeting

613 total reads per cell for 20,000 at minimum, and the sequencing cycles consisted of 28bp
614 for read 1, 90 bp for read 2, and 10 bp for i7 index, and 10bp for i5 index.
615 Count matrices were generated from the single-cell raw fastq files using 10x
616 genomics *cellranger* software (v.4.0) using hg38 reference genome provided by 10x
617 Genomics. We filtered the data to only include cells expressing at least 2000 detectable
618 genes (using "nFeature_RNA" filter); this also filtered out dead cells with >10% mt-DNA
619 gene expression in our data set. Our data coverage included approximately ~ 3000
620 genes in average of 5000 cells in each population. The resulting count matrices were
621 analyzed by Seurat package (v3.9.9) with the standard workflow (Butler *et al*, 2018;
622 Stuart *et al*, 2019). After applying the (*nFeature_RNA* > 2000), the expression data were
623 then normalized using the *NormalizeData* function in Seurat and variable featuresets
624 were identified using the *FindVariableFeatures* function in Seurat. Depending on the
625 type of comparison, specific sets of samples were combined using the *IntegrateData*
626 function. The integrated datasets were scaled and cells were clustered with up to 20
627 dimensions (dim=1:20). We performed clustering using several resolution parameters
628 (0.1-0.8) and visually selected optimal resolution for specific datasets. The clusters were
629 visualized using UMAP with up to 20 dimensions. Marker genes for each cluster were
630 calculated with the *FindAllMarkers* function and statistical significance was calculated by
631 Wilcoxon Rank Sum test. Differential expression of the cluster markers was carried out
632 using the FindMarkers function of Seurat. For this, we only used the normalized data
633 before integration (assay 'RNA') using the Wilcoxon rank sum test, as suggested by
634 Seurat documentation. For cell-cycle scoring, we use the CellCycleScoring function of
635 Seurat, which provides scores of G2M and S phase scores and assigns cell-cycle
636 phases based on these scores (Tirosh *et al*, 2016). The cell-lineage determination and
637 trajectory calculation were carried out using the *Slingshot* (Street *et al*, 2018) package
638 with Seurat clusters and default parameters. The algorithm was allowed to automatically
639 identify the start and the end clusters. GSEA analyses were performed with ranked log
640 fold change (LFC) of markers (>0.1, p<0.01) using MsigDB as described in (Tanwar et
641 al., 2016). Overrepresentation analyses were performed with genes with negative LFC
642 in Cluster 5 using the Reactome PA package of R v 3.6.0.

643

644 **Statistical analyses:**

645 Drawing of plots and statistical analyses were performed using Excel, SPSS or R
646 package as mentioned in appropriate section above.

647

648 **ACKNOWLEDGEMENTS:**

649 BS, KM, AM are supported by NIH award (# R33ES025662). We acknowledge Dezhi
650 Wang from the Pat Pathology Core Research Laboratory for preparation of H&E stained
651 slides, the UAB Flow Cytometry and Single Cell Services Core that is supported by
652 AR048311, AI027667, and the Dr. Mike Crowley from the Heflin Genomics Core for sc-
653 RNAseq.

654 **AUTHOR CONTRIBUTION**

655 BS designed and performed experiments and analyzed data along with AM and AG; DP
656 generated the transformed lines and performed basic characterization; ABH supervised
657 the xenograft experiments performed by BS and SG; GPS performed the pathological
658 evaluation of tumor sections; SL provided consultation for the sc-RNAseq and prepared
659 the scRNAseq library; MKB provided consultation for the sc-RNAsq analyses and
660 performed the analyses; KM conceived the study, helped in experimental design,
661 analyzed data and wrote the manuscript with BS.

662 **DECLARATION OF INTEREST**

663 The authors declare no competing interests.

664

665

666

667

668

669

FIGURE LEGENDS:

Figure 1. Keratinocytes transformed under mild carcinogenic stress exhibit attenuated Drp1 activity and have abundant self-renewing/proliferating cells. **A)** Cell proliferation assay (quantified by crystal violet staining) of HaCaT cells after exposure to TCDD (1 or 10 nM) over 4 and 16 days, with Toluene (10nM) as vehicle control. **B)** Immunoblot analyses of AHR and actin (loading control) in transformed HaCaT populations, TF-1 and TF-10, in the absence of TCDD. **C)** Representative micrographs (40X) of H&E stained sections of tumor xenografts formed by TF-1 and TF-10 HaCaT cells; zoom of boxed region shown in the bottom panels. **D)** Immunoblot analyses of Drp1, pDrp1(S616), Mfn1, Mfn2, Opa1 and actin (loading control) in TF-1 and TF-10 HaCaT cells. **E)** Maximum intensity projection of confocal optical sections of representative Parental, TF-1 and TF-10 HaCaT cells expressing mitoPSmO. **F)** Quantification of mitochondrial [Fission] and [Fusion5] metrics from micrographs represented in (E). **G)** Quantification of cell proliferation assay (as in A) of Parental, TF-1 and TF-10 HaCaT cells over 7 days in the absence of TCDD. **H)** Representative micrograph showing spheroids formed when 10^4 Parental, TF-1 or TF-10 HaCaT cells were maintained in low attachment plate in presence of stem cell medium. **I)** Quantification of spheroid forming frequency of Parental, TF-1 or TF-10 HaCaT cells using ELDA. * signifies p value of <0.05 in T test (A,F) and ELDA (I); scale bar depicts 10 μm (D) and 100 μm (H).

Figure. 2. Drp1 attenuated TF-1 keratinocyte population maintains an expanded slow-cycling subpopulation with elevated stem/progenitor cell markers. **A)** UMAP plot of scRNA-seq derived clusters (0-5) of Parental, TF-1 and TF-10 HaCaT cells (top); pie chart of the percentage distribution of the clusters (bottom, p value from ChiSquare test); color coded arrows point the clusters with unique reciprocal abundance in TF-1 cells. **B)** Violin plots depicting expression of Krt13, Krt15, Krt5, Sox2 and Sox4 in the clusters identified in (A) in the Parental, TF-1 and TF-10 HaCaT cells; color coded arrow point to Cluster 3 marked by Krts. **C)** Normalized Enrichment Scores (NES) of functional pathways identified by GSEA analyses of marker genes of Clusters 0-4 (Extended data Table 2) and by overrepresentation analyses for Cluster 5 (* represents categories

including mtDNA genes); functional categories defined by majority of the leading-edge genes are in parentheses, while clusters are arranged based on trajectory analyses (open arrows) (see Extended Fig. 2F). **D)** Violin plots depicting expression of cyclinA2, cyclinB1, CDK1, cyclinD2 and PCNA in the clusters identified in (A) in the Parental, TF-1 and TF-10 HaCaT cells; the functional category of genes identified in (C) is included in the cluster identity. **E)** Distribution of G2-M and S scores obtained by gene expression analyses of cell cycle predictive genes in the Parental, TF-1 and TF-10 HaCaT cells. **F)** Feature plot of G2-M and S scores obtained from (E). **G)** Bar plot showing fraction of cells in G2-M, S and G0/G1, computed from (E) in the functionally categorized clusters in the Parental, TF-1 and TF-10 HaCaT cells; inset shows G1 to S reciprocity of the clusters (color-coded arrows) with unique reciprocal abundance in TF-1 cells in (A).

Figure 3. Fine-tuned repression of Drp1 sustains a [CyclinE^{hi}-Sox2^{hi}-Krt15^{hi}] state and accelerates carcinogen driven cell transformation. **A)** Immunoblot analyses of Sox2, Krt15 and actin (loading control) in Parental and TF-1 and TF-10 HaCaT cells. **B)** Dot plot of [Sox2] and [Krt15] levels obtained from confocal micrographs of co-immunostained Parental and TF-1 HaCaT cells; black lines, marking 4 quadrants, represent levels of Sox2 and Krt15 determined from normalized signal in each population (see Extended Fig. 3B). **C)** Dot plot of [Sox2] and [Drp1] levels obtained from confocal micrographs of co-immunostained Parental and TF-1 HaCaT cells; dotted lines mark the levels of [Drp1] in cells expressing higher [Sox2] levels. **D)** Dot plot of [Sox2] and [pDrp1(S616)] levels obtained from confocal micrographs of co-immunostained Parental and TF-1 HaCaT cells; dotted lines mark the levels of [pDrp1(S616)] in cells expressing higher [Sox2] levels. **E)** Immunoblot analyses of Drp1, Krt15, Sox2 and actin (loading control) in Parental HaCaT cells expressing non-targeted shRNA (Cnt), weaker (W) or stronger (S) Drp1 shRNA. **F)** Immunoblot analyses of Cyclins E1, E2, A2, B1, D2 and actin (loading control) in Parental and stable TF-1 and TF-10 HaCaT cells. **G)** Representative confocal micrographs of Cyclin E1 immunostaining in Parental and TF-1 HaCaT cells; N depict the nucleus in each cell identified by DNA stain (not shown). **H)** Box plot showing quantification of nuclear to cytosolic ratio of Cyclin E1 levels quantified from experiment described in (G). **I)** Dot plot of [Sox2] and [CyclinE1(pT62)] levels

obtained from confocal micrographs of co-immunostained Parental and TF-1 HaCaT cells; dotted lines mark the levels of [CyclinE1(pT62)] in cells expressing higher [Sox2] levels. **J)** Representative images of Cyclin E1 immunostaining in Parental HaCat cells expressing non-targeted shRNA (Cnt), weaker (W) or stronger (S) Drp1 shRNA. **K)** Box plot showing quantification of nuclear to cytosolic ratio of Cyclin E1 levels quantified from experiment described in (J). **L)** Cell proliferation assay of Parental HaCaT cells expressing non-targeted shRNA (Cnt), weaker (W) or stronger (S) Drp1 shRNA after exposure to TCDD (1nM or 10nM) at an early and a late time point in the neoplastic transformation protocol; 'Toluene' is the vehicle control for TCDD and 'Control' is with no chemical. * signifies p value of <0.05 in KW (G) and T test (L); scale bar depicts 20 μm.

Figure 4. Fine-tuned repression of Drp1 maintains smaller fused mitochondrial elements, and sustains transcriptomic profile similar to the neoplastic stem cell enriched TF-1 population. A) Dot plot of [Fission] and [Fusion5] obtained from confocal micrographs of Mitotracker green stained live Parental HaCaT cells expressing non-targeted shRNA as control (Cnt), weaker (W) or stronger (S) Drp1 shRNA; numbers denote the percentage of cells in the adjacent boxes with p value from ChiSquare test; representative images in Extended Fig. 3D **B)** Dot plot of [Fission] or [Fusion5] of single cells (from A) with their total mitochondrial number and total mitochondrial length; lines represent the ranges of [Fission] and [Fusion5] to demarcate cell subpopulations in boxes in (A). **C)** Bar graph signifying percentage of cells from (A) with >80 [Fusion1] metric (top); dot plot of [Fission] and [Fusion1] of cells from (A) (bottom). **D)** Barplots showing positive and negative log fold change values of top 20 genes in Parental HaCaT cells expressing weaker (W) (Top) or stronger (S) (bottom) shRNA with respect to the cells expressing non-targeting shRNA (Cnt); 0 signifies no change and color coded * denote relevant Krt genes. **E)** Barplot showing ratio of absolute expression values of mitochondrial genes (top) and ribosomal or protein translation genes (bottom) in the Parental HaCat cells expressing the stronger (S) or the weaker (W) Drp1 shRNA with respect to those expressing non-targeting shRNA (Cnt); 1 signifies no change. **F)** Line plot showing % population of Parental cells expressing the strong (S) or weak (W)

763 Drp1 shRNA in the named scRNA-seq derived cell clusters, with respect to those
764 expressing non-targeting shRNA (Cnt). This is compared to the same in the TF-1 cells
765 with respect to its Parental population; 1 signifies no change from respective control. **G)**
766 Distribution of G2-M and S scores obtained by gene expression analyses of cell cycle
767 predictive genes in the Parental HaCaT cells expressing non-targeted shRNA (Cnt),
768 weaker Drp1-shRNA (W) or stronger shRNA (S). **H)** Violin plots depicting expression of
769 cyclinB1, CDK1 (left panel) and cyclinD2, PCNA (right panel) in the named scRNA-seq
770 derived cell clusters in the Parental HaCaT cells expressing non-targeted shRNA (Cnt),
771 weaker Drp1-shRNA (W) or stronger shRNA (S).
772
773 **Figure. 5. Proposed model of a 'Goldilocks' zone of Drp1 activity for priming a**
774 **stem/progenitor like state to accelerate neoplastic transformation.** In a
775 keratinocyte model, a level of fine-tuned repression (ftr) of Drp1 maintains smaller fused
776 mitochondrial networks and sustains a state of [$Drp1^{ftr}$-$CyclinE^{hi}$-$Sox2^{hi}$-$Krt15^{+}$], which is
777 susceptible to carcinogen (TCDD) driven neoplastic transformation. Low dose of TCDD
778 driven transformation leads to a similar Drp1 attenuated (att) state of [$Drp1^{att}$-$CyclinE^{hi}$-
779 $Sox2^{hi}$-$Krt15^{+}$] that forms less differentiated (primitive) tumors, while a 10-fold higher
780 TCDD dose transforms cells to a state of [$Drp1^{hi}$-$CyclinE^{lo}$-$Sox2^{lo}$-$Krt15^{+}$] that forms
781 differentiated tumors. Supra optimal repression of Drp1 maintains hyperfused
782 mitochondria and sustains a state of [$Drp1^{lo}$-$CyclinE^{hi}$-$Sox2^{hi}$-$Krt15^{-}$], which prevents
783 carcinogen driven neoplastic transformation.
784
785
786
787
788
789
790
791
792
793
794

EXTENDED FIGURE LEGENDS:

Extended Figure 1. A) Quantification of incidence and volume of xenograft tumors formed by TF-1 and TF-10 HaCaT cells; # indicates presence of a distant tumor. **B)** Immunoblot analyses of Cytochrome C, Fis1, Tom20 and actin (loading control) in Parental and TF-1 and TF-10 HaCaT cells.

Extended Figure 2. A) Bar plot showing the percentage distribution of the clusters (0-5) in each of the cell populations identified by scRNA-seq analyses of Parental, TF-1 and TF-10 HaCat cells (left); numbers show cell cycle distribution from flowcytometry analyses of PI stained cells in the corresponding population (right). **B)** UMAP plot of scRNA-seq derived clusters (0-5) of Parental, TF-1 and TF-10 HaCaT cells obtained with minimum cluster resolution; color coded arrows point the major change in cluster distribution in transformed cells. **C)** Heat map of statistically significant marker genes for the color-coded clusters (0-5) of Parental, TF-1 and TF-10 HaCaT cells; color coded arrows point to the top most marker gene in the 3 clusters that are have different distribution between the Parental and transformed populations; color index shows log fold change; * marks the Histone gene cluster. **D)** Violin plots depicting expression of the mt-DNA genes in the named scRNA-seq derived cell clusters in the Parental, TF-1 and TF-10 HaCaT cells. **E)** Violin plots depicting expression of HES1 and OASL genes in the named scRNA-seq derived cell clusters in the Parental, TF-1 and TF-10 HaCaT cells. **F)** PCA plot of trajectory analyses of the scRNA-seq derived cell clusters in the Parental, TF-1 and TF-10 HaCaT cells.

Extended Figure 3. A) Representative confocal micrographs of immunostained Parental and TF-1 HaCaT cells showing endogenous expression of Oct4, Nanog and Sox2; blue depicting nuclear staining with Hoechst. **B)** Dot plot of [Sox2] and [Krt15] obtained from confocal micrographs of co-immunostained Parental and TF-1 HaCaT cells; [Sox2] levels normalized to the minimum in the respective population (left) and [Krt15] levels normalized to the minimum in the respective population (right); black lines demarcate levels of Sox2 and Krt15 as determined from the normalized signal of the other. **C)** Representative confocal micrographs of Parental and TF-1 HaCaT cells showing endogenous expression of Tom20 and Cyclin E1 after 2 hours incubation with

DMSO or Cychloheximide, with the pre-incubation time point (0h) as control. **D)** Representative maximum intensity projections (MIP) of confocal optical sections (micrograph) and the corresponding MitoGraph generated binary images (binary) for quantifying [Fission] and [Fusion1/5] metrics of the Parental HaCaT cells expressing non-targeted shRNA (Cnt), strong (S) or weak (W) Drp1 shRNA; the cells represent populations in colored boxes in Fig. 4A while the number depicts their abundance in percentage. Scale bar depicts 100 μm (A, C) or 15 μm (D).

Extended Figure 4. A) Bar plot showing the knockdown efficiency of strong (S) or weak (W) Drp1 shRNA expressed as ratio of Drp1 transcript levels in the knockdown HaCaT and that of the cells expressing the non-targeted shRNA control. **B)** Bar plot showing log fold change of overall gene expression of Parental HaCaT cells expressing strong (S) or weak (W) Drp1 shRNA with respect to those expressing the non-targeted shRNA (Cnt). **C)** Plots showing ratio of the expression of covered genes between the Parental HaCaT cells expressing strong (S) or weak (W) Drp1 shRNA; “Similar effects” showing ratio of increase or decrease in the (S) Drp1 shRNA over the (W) Drp1 shRNA (back arrows in left panel), while opposite effects showing opposite trends in genes as labelled in the arrows (back arrows right panel); grey arrows point to the top 20 genes of each category. **D)** UMAP plot of scRNA-seq based clusters (0-5) of Parental HaCaT cells expressing non-targeted shRNA (Cnt), strong (S) or weak (W) Drp1 shRNA; arrow pointing the SloCyc-Krt15-hi cluster (note color coding is not same as the one presented in Fig. 2). **E)** Bar plot showing percentage of statistically significant common genes (Upregulated or Downregulated) between color coded clusters obtained with the scRNA-seq data set of parental and transformed HaCaT cells (Fig. 2) and that of parental expressing control or Drp1 shRNAs (Fig. 4); same color coding is maintained between the two data sets. **F)** Violin plots depicting expression of Krt13, Krt15, Krt4, Krt5, Krt6A, Krt7 genes in the named scRNA-seq based cell clusters in the Parental HaCaT cells expressing non-targeted shRNA (Cnt), strong (S) or weak (W) Drp1 shRNA. **G)** Bar plot showing fraction of cells in G2-M, S and G0/G1, computed from main Fig. 4G, in the functionally categorized clusters in the Parental cells expressing non-targeted shRNA (Cnt), strong (S) or weak (W) Drp1 shRNA.

REFERENCES

Boelsma E, Verhoeven MC, Ponec M (1999) Reconstruction of a human skin equivalent using a spontaneously transformed keratinocyte cell line (HaCaT). J Invest Dermatol 112: 489-98

Bonnay F, Veloso A, Steinmann V, Kocher T, Abdusselamoglu MD, Bajaj S, Rivelles E, Landskron L, Esterbauer H, Zinzen RP, Knoblich JA (2020) Oxidative Metabolism Drives Immortalization of Neural Stem Cells during Tumorigenesis. Cell 182: 1490-1507 e19

Boumahdi S, Driessens G, Lapouge G, Rorive S, Nassar D, Le Mercier M, Delatte B, Caauwe A, Lenglez S, Nkusi E, Brohee S, Salmon I, Dubois C, del Marmol V, Fuks F, Beck B, Blanpain C (2014) SOX2 controls tumour initiation and cancer stem-cell functions in squamous-cell carcinoma. Nature 511: 246-50

Butler A, Hoffman P, Smibert P, Papalexi E & Satija R (2018) Integrating single-cell transcriptomic data across different conditions, technologies, and species. *Nature Biotechnology* 36: 411–420

Chen H, Chan DC (2017) Mitochondrial Dynamics in Regulating the Unique Phenotypes of Cancer and Stem Cells. Cell Metab 26: 39-48

Der Vartanian A, Quetin M, Michineau S, Aurade F, Hayashi S, Dubois C, Rocancourt D, Drayton-Libotte B, Szegedi A, Buckingham M, Conway SJ, Gervais M, Relaix F (2019) PAX3 Confers Functional Heterogeneity in Skeletal Muscle Stem Cell Responses to Environmental Stress. Cell Stem Cell 24: 958-973 e9

Di Meglio P, Duarte JH, Ahlfors H, Owens ND, Li Y, Villanova F, Tosi I, Hirota K, Nestle FO, Mrowietz U, Gilchrist MJ, Stockinger B (2014) Activation of the aryl hydrocarbon receptor dampens the severity of inflammatory skin conditions. Immunity 40: 989-1001

Favaro G, Romanello V, Varanita T, Andrea Desbats M, Morbidoni V, Tezze C, Albiero M, Canato M, Gherardi G, De Stefani D, Mammucari C, Blaauw B, Boncompagni S, Protasi F, Reggiani C, Scorrano L, Salviati L, Sandri M (2019) DRP1-mediated mitochondrial shape controls calcium homeostasis and muscle mass. Nat Commun 10: 2576

Folmes CD, Dzeja PP, Nelson TJ, Terzic A (2012) Metabolic plasticity in stem cell homeostasis and differentiation. Cell Stem Cell 11: 596-606

Foronda M, Martinez P, Schoeftner S, Gomez-Lopez G, Schneider R, Flores JM, Pisano DG, Blasco MA (2014) Sox4 links tumor suppression to accelerated aging in mice by modulating stem cell activation. Cell Rep 8: 487-500

Friedman JR, Nunnari J (2014) Mitochondrial form and function. Nature 505: 335-43

Fuchs E (2016) Epithelial Skin Biology: Three Decades of Developmental Biology, a Hundred Questions Answered and a Thousand New Ones to Address. Curr Top Dev Biol 116: 357-74

Geng Y, Yu Q, Sicinska E, Das M, Schneider JE, Bhattacharya S, Rideout WM, Bronson RT, Gardner H, Sicinski P (2003) Cyclin E ablation in the mouse. Cell 114: 431-43

Giroux V, Lento AA, Islam M, Pitarresi JR, Kharbanda A, Hamilton KE, Whelan KA, Long A, Rhoades B, Tang Q, Nakagawa H, Lengner CJ, Bass AJ, Wileyto EP, Klein-Szanto AJ, Wang TC, Rustgi AK (2017) Long-lived keratin 15+ esophageal progenitor cells contribute to homeostasis and regeneration. J Clin Invest 127: 2378-2391

Gonzales KAU, Fuchs E (2017) Skin and Its Regenerative Powers: An Alliance between Stem Cells and Their Niche. Dev Cell 43: 387-401

Hao N, Lee KL, Furness SG, Bosdotter C, Poellinger L, Whitelaw ML (2012) Xenobiotics and loss of cell adhesion drive distinct transcriptional outcomes by aryl hydrocarbon receptor signaling. Mol Pharmacol 82: 1082-93

Hoppins S (2014) The regulation of mitochondrial dynamics. Curr Opin Cell Biol 29: 46-52

Hu Y, Smyth GK (2009) ELDA: extreme limiting dilution analysis for comparing depleted and enriched populations in stem cell and other assays. J Immunol Methods 347: 70-8

Hwang HC, Clurman BE (2005) Cyclin E in normal and neoplastic cell cycles. Oncogene 24: 2776-86

Iwata R, Casimir P, Vanderhaeghen P (2020) Mitochondrial dynamics in postmitotic cells regulate neurogenesis. Science 369: 858-862

Jung MH, Jung SM, Shin HS (2016) Co-stimulation of HaCaT keratinization with mechanical stress and air-exposure using a novel 3D culture device. Sci Rep 6: 33889

Kageyama Y, Zhang Z, Sesaki H (2011) Mitochondrial division: molecular machinery and physiological functions. Curr Opin Cell Biol 23: 427-34

Karantza V (2011) Keratins in health and cancer: more than mere epithelial cell markers. Oncogene 30: 127-38

Kashatus JA, Nascimento A, Myers LJ, Sher A, Byrne FL, Hoehn KL, Counter CM, Kashatus DF (2015) Erk2 phosphorylation of Drp1 promotes mitochondrial fission and MAPK-driven tumor growth. Mol Cell 57: 537-51

948 Khacho M, Clark A, Svoboda DS, Azzi J, MacLaurin JG, Meghaizel C, Sesaki H,
949 Lagace DC, Germain M, Harper ME, Park DS, Slack RS (2016) Mitochondrial Dynamics
950 Impacts Stem Cell Identity and Fate Decisions by Regulating a Nuclear Transcriptional
951 Program. Cell Stem Cell 19: 232-247
952
953 Khacho M, Slack RS (2017) Mitochondrial activity in the regulation of stem cell self-
954 renewal and differentiation. Curr Opin Cell Biol 49: 1-8
955
956 Leclerc D, Staats Pires AC, Guillemin GJ, Gilot D (2021) Detrimental activation of AhR
957 pathway in cancer: an overview of therapeutic strategies. Curr Opin Immunol 70: 15-26
958
959 Li S, Park H, Trempus CS, Gordon D, Liu Y, Cotsarelis G, Morris RJ (2013) A keratin 15
960 containing stem cell population from the hair follicle contributes to squamous papilloma
961 development in the mouse. Mol Carcinog 52: 751-9
962
963 Liang R, Arif T, Kalmykova S, Kasianov A, Lin M, Menon V, Qiu J, Bernitz JM, Moore K,
964 Lin F, Benson DL, Tzavaras N, Mahajan M, Papatsenko D, Ghaffari S (2020)
965 Restraining Lysosomal Activity Preserves Hematopoietic Stem Cell Quiescence and
966 Potency. Cell Stem Cell 26: 359-376 e7
967
968 Lisowski P, Kannan P, Mlody B, Prigione A (2018) Mitochondria and the dynamic
969 control of stem cell homeostasis. EMBO Rep 19
970
971 Liu L, Michowski W, Kolodziejczyk A, Sicinski P (2019) The cell cycle in stem cell
972 proliferation, pluripotency and differentiation. Nat Cell Biol 21: 1060-1067
973
974 Luecken MD, Theis FJ (2019) Current best practices in single-cell RNA-seq analysis: a
975 tutorial. Mol Syst Biol 15: e8746
976
977 Maga G, Hubscher U (2003) Proliferating cell nuclear antigen (PCNA): a dancer with
978 many partners. J Cell Sci 116: 3051-60
979
980 Magee JA, Piskounova E, Morrison SJ (2012) Cancer stem cells: impact, heterogeneity,
981 and uncertainty. Cancer Cell 21: 283-96
982
983 Mandal S, Freije WA, Guptan P, Banerjee U (2010) Metabolic control of G1-S transition:
984 cyclin E degradation by p53-induced activation of the ubiquitin-proteasome system. J
985 Cell Biol 188: 473-9
986
987 Mitra K, Lippincott-Schwartz J (2010) Analysis of mitochondrial dynamics and functions
988 using imaging approaches. Curr Protoc Cell Biol Chapter 4: Unit 4 25 1-21
989
990 Mitra K, Rikhy R, Lilly M, Lippincott-Schwartz J (2012) DRP1-dependent mitochondrial
991 fission initiates follicle cell differentiation during Drosophila oogenesis. J Cell Biol 197:
992 487-97
993

Mitra K, Wunder C, Roysam B, Lin G, Lippincott-Schwartz J (2009) A hyperfused mitochondrial state achieved at G1-S regulates cyclin E buildup and entry into S phase. Proc Natl Acad Sci U S A 106: 11960-5

Moriyama M, Durham AD, Moriyama H, Hasegawa K, Nishikawa S, Radtke F, Osawa M (2008) Multiple roles of Notch signaling in the regulation of epidermal development. Dev Cell 14: 594-604

Morris RJ, Liu Y, Marles L, Yang Z, Trempus C, Li S, Lin JS, Sawicki JA, Cotsarelis G (2004) Capturing and profiling adult hair follicle stem cells. Nat Biotechnol 22: 411-7

Mulero-Navarro S, Fernandez-Salguero PM (2016) New Trends in Aryl Hydrocarbon Receptor Biology. Front Cell Dev Biol 4: 45

Nagdas S, Kashatus JA, Nascimento A, Hussain SS, Trainor RE, Pollock SR, Adair SJ, Michaels AD, Sesaki H, Stelow EB, Bauer TW, Kashatus DF (2019) Drp1 Promotes KRas-Driven Metabolic Changes to Drive Pancreatic Tumor Growth. Cell Rep 28: 1845-1859 e5

Orford KW, Scadden DT (2008) Deconstructing stem cell self-renewal: genetic insights into cell-cycle regulation. Nat Rev Genet 9: 115-28

Otsuki L, Brand AH (2018) Cell cycle heterogeneity directs the timing of neural stem cell activation from quiescence. Science 360: 99-102

Parker DJ, Iyer A, Shah S, Moran A, Hjelmeland AB, Basu MK, Liu R, Mitra K (2015) A new mitochondrial pool of cyclin E, regulated by Drp1, is linked to cell-density-dependent cell proliferation. J Cell Sci 128: 4171-82

Pauklin S, Vallier L (2013) The cell-cycle state of stem cells determines cell fate propensity. Cell 155: 135-47

Prieto J, Leon M, Ponsoda X, Sendra R, Bort R, Ferrer-Lorente R, Raya A, Lopez-Garcia C, Torres J (2016) Early ERK1/2 activation promotes DRP1-dependent mitochondrial fission necessary for cell reprogramming. Nat Commun 7: 11124

Purba TS, Haslam IS, Poblet E, Jimenez F, Gandarillas A, Izeta A, Paus R (2014) Human epithelial hair follicle stem cells and their progeny: current state of knowledge, the widening gap in translational research and future challenges. Bioessays 36: 513-25

Ray SS, Swanson HI (2004) Dioxin-induced immortalization of normal human keratinocytes and silencing of p53 and p16INK4a. J Biol Chem 279: 27187-93

Ryan MT, Hoogenraad NJ (2007) Mitochondrial-nuclear communications. Annu Rev Biochem 76: 701-22

Sang L, Coller HA, Roberts JM (2008) Control of the reversibility of cellular quiescence by the transcriptional repressor HES1. Science 321: 1095-100

Schaefer T, Lengerke C (2020) SOX2 protein biochemistry in stemness, reprogramming, and cancer: the PI3K/AKT/SOX2 axis and beyond. Oncogene 39: 278-292

Schoop VM, Mirancea N, Fusenig NE (1999) Epidermal organization and differentiation of HaCaT keratinocytes in organotypic coculture with human dermal fibroblasts. J Invest Dermatol 112: 343-53

Schrepfer E, Scorrano L (2016) Mitofusins, from Mitochondria to Metabolism. Mol Cell 61: 683-694

Senos Demarco R, Uyemura BS, D'Alterio C, Jones DL (2019) Mitochondrial fusion regulates lipid homeostasis and stem cell maintenance in the Drosophila testis. Nat Cell Biol 21: 710-720

Serasinghe MN, Wieder SY, Renault TT, Elkholi R, Asciolla JJ, Yao JL, Jabado O, Hoehn K, Kageyama Y, Sesaki H, Chipuk JE (2015) Mitochondrial division is requisite to RAS-induced transformation and targeted by oncogenic MAPK pathway inhibitors. Mol Cell 57: 521-36

Seykora JT, Cotsarelis G (2011) Keratin 15-positive stem cells give rise to basal cell carcinomas in irradiated Ptch1(+/-) mice. Cancer Cell 19: 5-6

Siegle JM, Basin A, Sastre-Perona A, Yonekubo Y, Brown J, Sennett R, Rendl M, Tsirigos A, Carucci JA, Schober M (2014) SOX2 is a cancer-specific regulator of tumour initiating potential in cutaneous squamous cell carcinoma. Nat Commun 5: 4511

Simpson CL, Tokito MK, Uppala R, Sarkar MK, Gudjonsson JE, Holzbaur ELF (2021) NIX initiates mitochondrial fragmentation via DRP1 to drive epidermal differentiation. Cell Rep 34: 108689

Siu KT, Rosner MR, Minella AC (2012) An integrated view of cyclin E function and regulation. Cell Cycle 11: 57-64

Spurlock B, Gupta P, Basu MK, Mukherjee A, Hjelmeland AB, Darley-Usmar V, Parker D, Foxall ME, Mitra K (2019) New quantitative approach reveals heterogeneity in mitochondrial structure-function relations in tumor initiating cells. J Cell Sci

Spurlock B, Tullet J, Hartman JLt, Mitra K (2020) Interplay of mitochondrial fission-fusion with cell cycle regulation: Possible impacts on stem cell and organismal aging. Exp Gerontol 135: 110919

Spurlock B and Mitra K (2021a) Methods Molecular Biology, Vol. 2275, Volkmar Weissig and Marvin Edeas (Eds): Mitochondrial Medicine , 978-1-0716-1261-3, 482923_2_En, (Chapter 27).

Spurlock B, Hanumanthu VS and Mitra K (2021b). Strategy of Isolating 'Primed' Tumor Initiating Cells Based on Mitochondrial Transmembrane Potential. Bio-protocol online, inPress.

St John LS, Sauter ER, Herlyn M, Litwin S, Adler-Storthz K (2000) Endogenous p53 gene status predicts the response of human squamous cell carcinomas to wild-type p53. Cancer Gene Ther 7: 749-56

Street K, Risso D, Fletcher RB, Das D, Ngai J, Yosef N, Purdom E & Dudoit S (2018) Slingshot: cell lineage and pseudotime inference for single-cell transcriptomics. *BMC Genomics* 19: 477

Stuart T, Butler A, Hoffman P, Hafemeister C, Papalexi E, Mauck WM, Hao Y, Stoeckius M, Smibert P & Satija R (2019) Comprehensive Integration of Single-Cell Data. *Cell* 177: 1888-1902.e21

Subramanian A, Tamayo P, Mootha VK, Mukherjee S, Ebert BL, Gillette MA, Paulovich A, Pomeroy SL, Golub TR, Lander ES, Mesirov JP (2005) Gene set enrichment analysis: a knowledge-based approach for interpreting genome-wide expression profiles. Proc Natl Acad Sci U S A 102: 15545-50

Tirosh I, Izar B, Prakadan SM, Wadsworth MH, Treacy D, Trombetta JJ, Rotem A, Rodman C, Lian C, Murphy G, *et al* (2016) Dissecting the multicellular ecosystem of metastatic melanoma by single-cell RNA-seq. *Science* 352: 189–196

Tanwar DK, Parker DJ, Gupta P, Spurlock B, Alvarez RD, Basu MK, Mitra K (2016) Crosstalk between the mitochondrial fission protein, Drp1, and the cell cycle is identified across various cancer types and can impact survival of epithelial ovarian cancer patients. Oncotarget 7: 60021-60037

Teixeira LK, Reed SI (2017) Cyclin E Deregulation and Genomic Instability. Adv Exp Med Biol 1042: 527-547

Tsuyoshi H, Orisaka M, Fujita Y, Asare-Werehene M, Tsang BK, Yoshida Y (2020) Prognostic impact of Dynamin related protein 1 (Drp1) in epithelial ovarian cancer. BMC Cancer 20: 467

van Velthoven CTJ, Rando TA (2019) Stem Cell Quiescence: Dynamism, Restraint, and Cellular Idling. Cell Stem Cell 24: 213-225

Twig G, Shirihai OS (2011) The interplay between mitochondrial dynamics and mitophagy. Antioxid Redox Signal 14: 1939-51

Vantaggiato C, Castelli M, Giovarelli M, Orso G, Bassi MT, Clementi E, De Palma C (2019) The Fine Tuning of Drp1-Dependent Mitochondrial Remodeling and Autophagy Controls Neuronal Differentiation. Front Cell Neurosci 13: 120

Wincent E, Bengtsson J, Mohammadi Bardbori A, Alsberg T, Luecke S, Rannug U, Rannug A (2012) Inhibition of cytochrome P4501-dependent clearance of the endogenous agonist FICZ as a mechanism for activation of the aryl hydrocarbon receptor. Proc Natl Acad Sci U S A 109: 4479-84

Wu MJ, Chen YS, Kim MR, Chang CC, Gampala S, Zhang Y, Wang Y, Chang CY, Yang JY, Chang CJ (2019) Epithelial-Mesenchymal Transition Directs Stem Cell Polarity via Regulation of Mitofusin. Cell Metab 29: 993-1002 e6

Xie Q, Wu Q, Horbinski CM, Flavahan WA, Yang K, Zhou W, Dombrowski SM, Huang Z, Fang X, Shi Y, Ferguson AN, Kashatus DF, Bao S, Rich JN (2015) Mitochondrial control by DRP1 in brain tumor initiating cells. Nat Neurosci 18: 501-10

Zerjatke T, Gak IA, Kirova D, Fuhrmann M, Daniel K, Gonciarz M, Muller D, Glauche I, Mansfeld J (2017) Quantitative Cell Cycle Analysis Based on an Endogenous All-in-One Reporter for Cell Tracking and Classification. Cell Rep 19: 1953-1966

Zhang H, Menzies KJ, Auwerx J (2018) The role of mitochondria in stem cell fate and aging. Development 145

Zhao Q, Yan S, Lu J, Parker DJ, Wu H, Sun Q, Crossman DK, Liu S, Wang Q, Sesaki H, Mitra K, Liu K, Jiao K (2021) Mitochondrial Fission Regulates Transcription of Ribosomal Protein Genes in Embryonic Hearts
bioRxiv 2021.02.10.430627; doi: https://doi.org/10.1101/2021.02.10.430627

Zhong X, Cui P, Cai Y, Wang L, He X, Long P, Lu K, Yan R, Zhang Y, Pan X, Zhao X, Li W, Zhang H, Zhou Q, Gao P (2019) Mitochondrial Dynamics Is Critical for the Full Pluripotency and Embryonic Developmental Potential of Pluripotent Stem Cells. Cell Metab 29: 979-992 e4

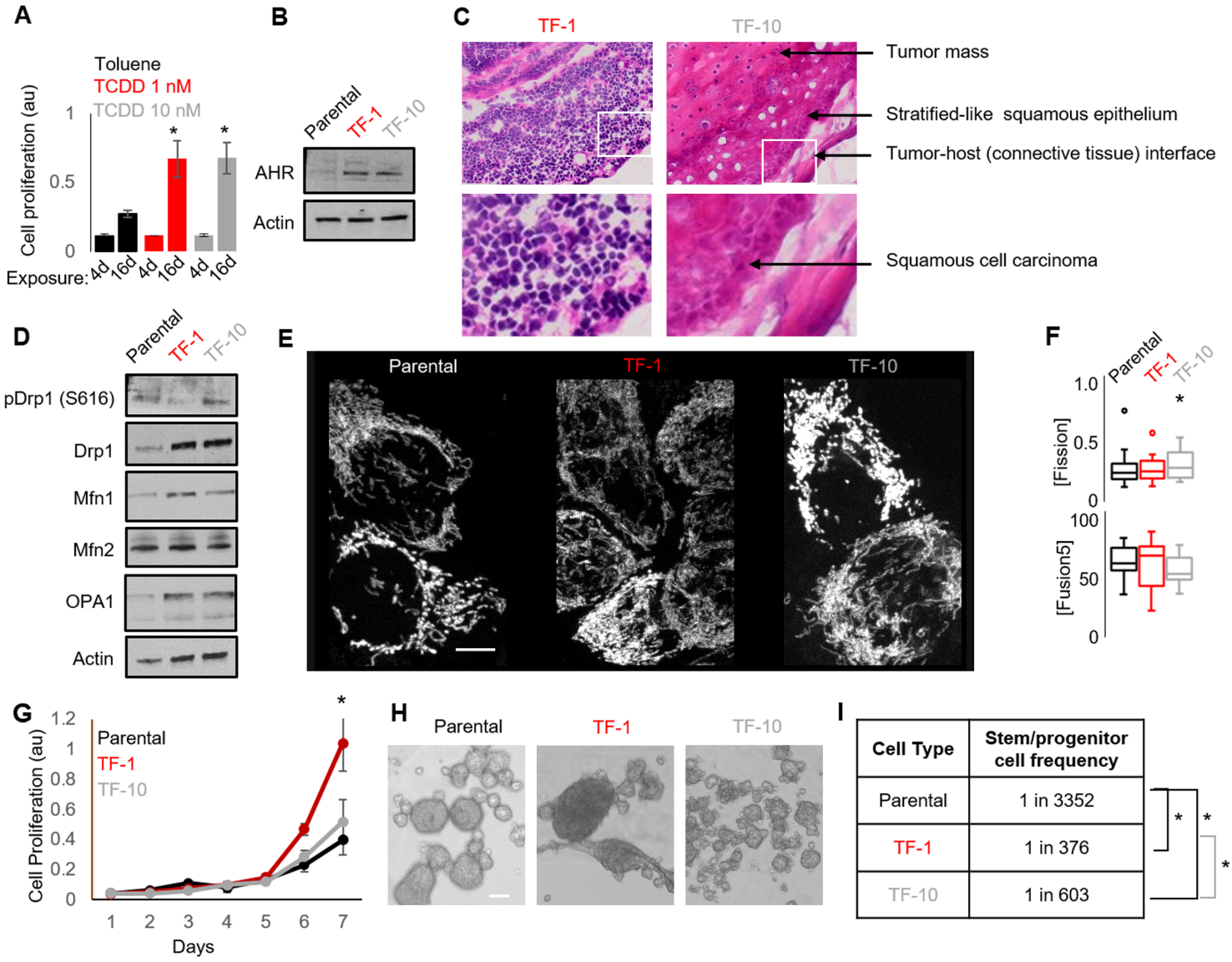

Figure. 1

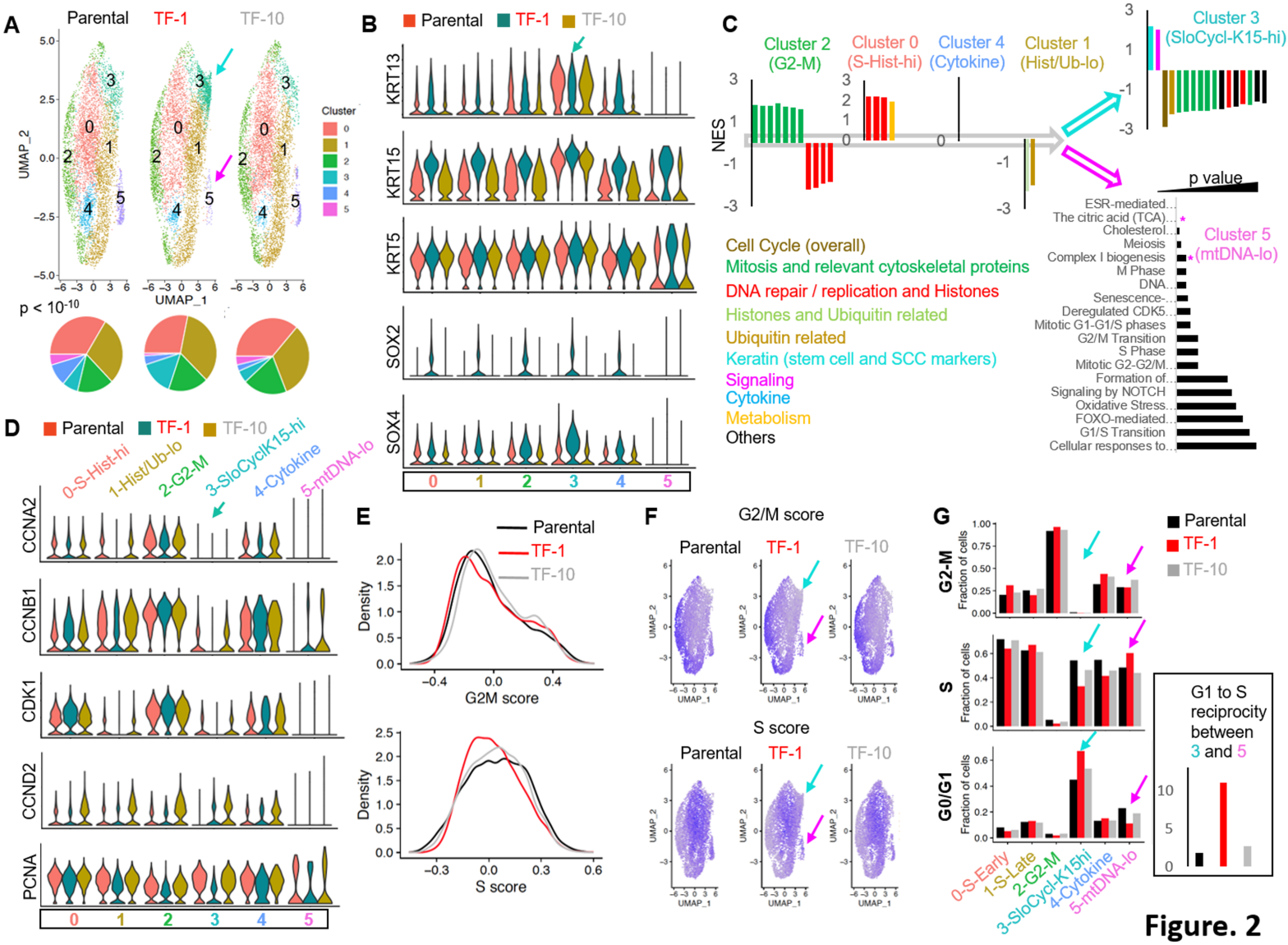

Figure. 2

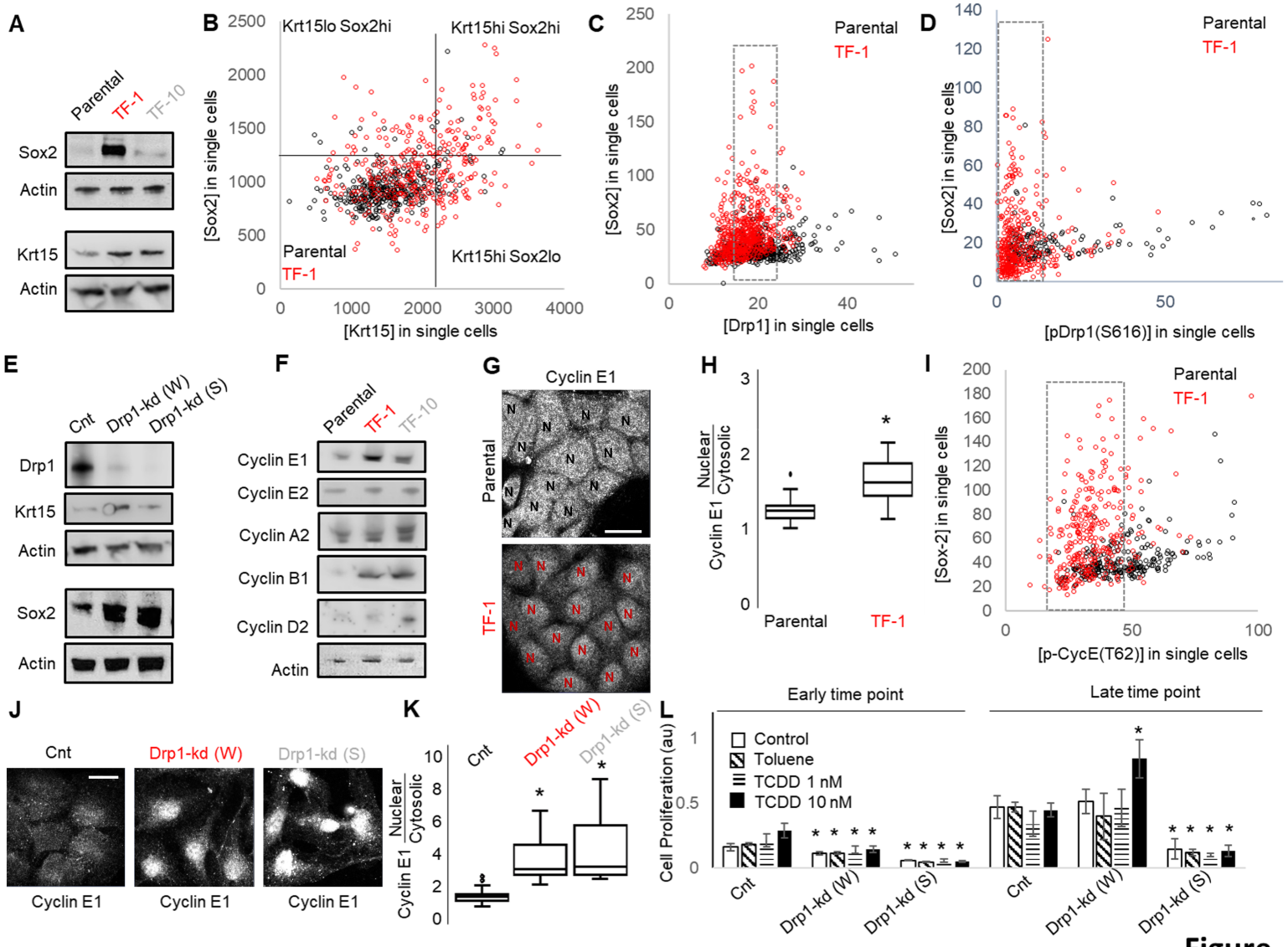

Figure. 3

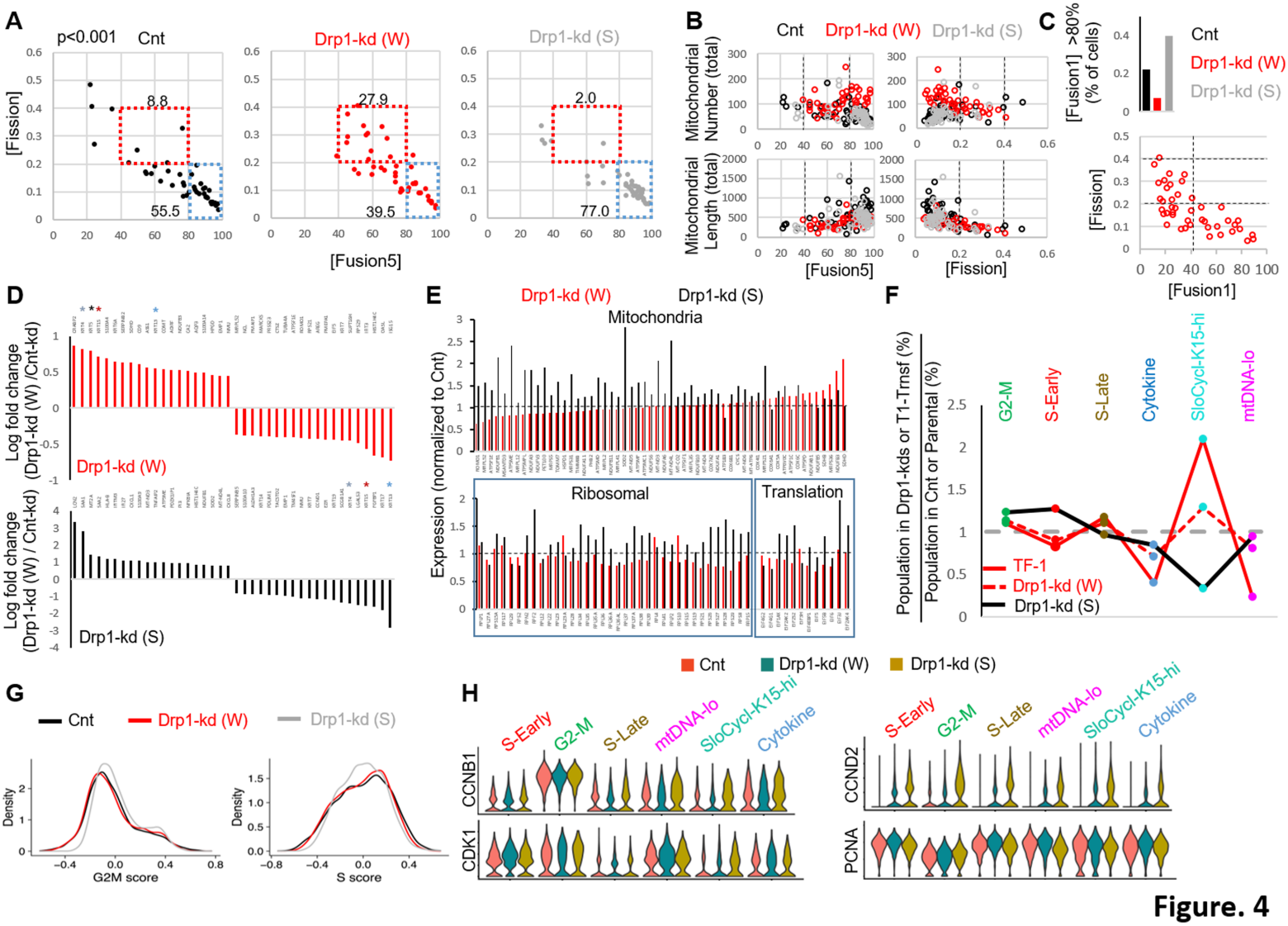

Figure. 4

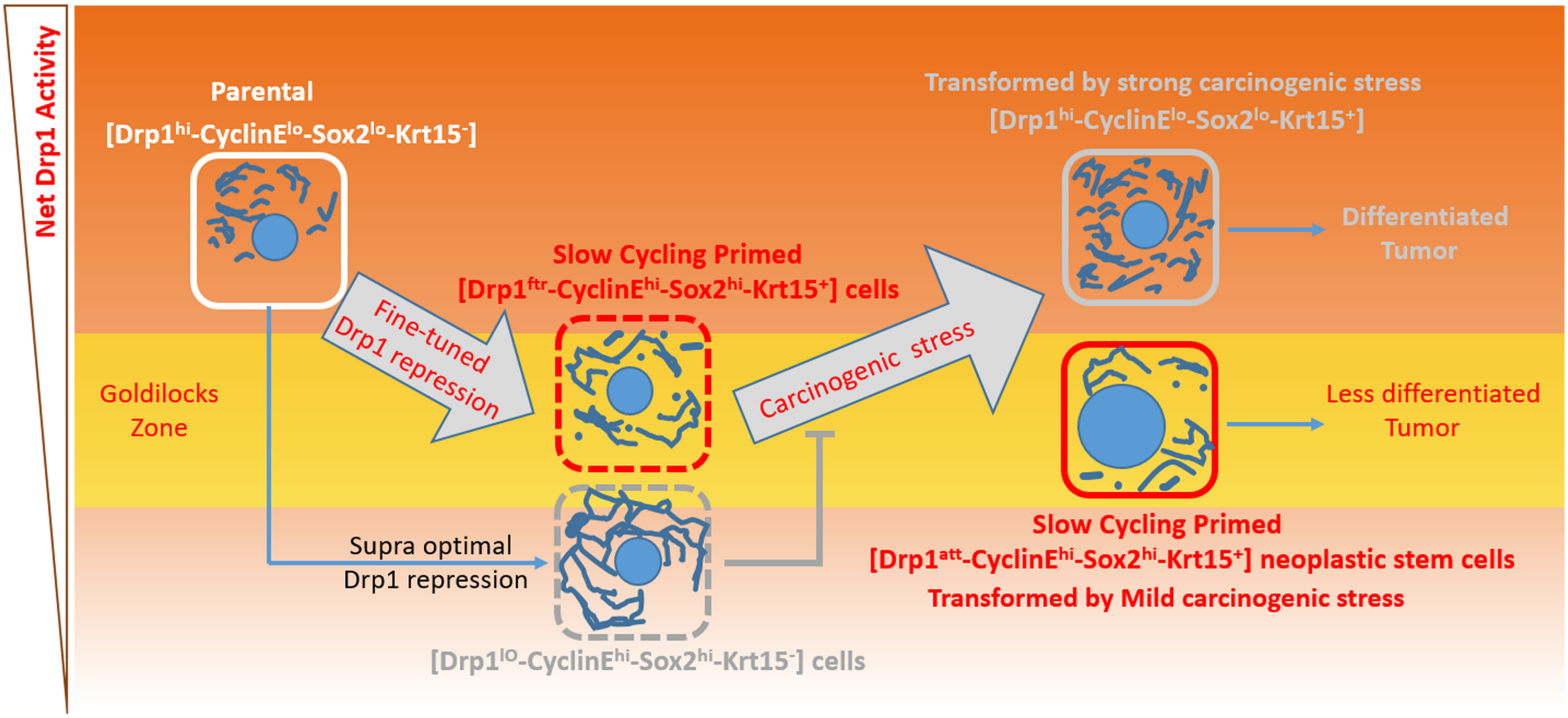

Figure. 5

A

Cells Injected	Tumor incidence	Tumor volume
Parental	0/9	N.A.
TF-1	#1/9	188.1 #363.1
TF-10	3/9	287.9 ± 173

B

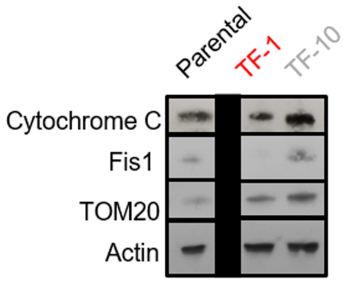

Extended Fig. 1

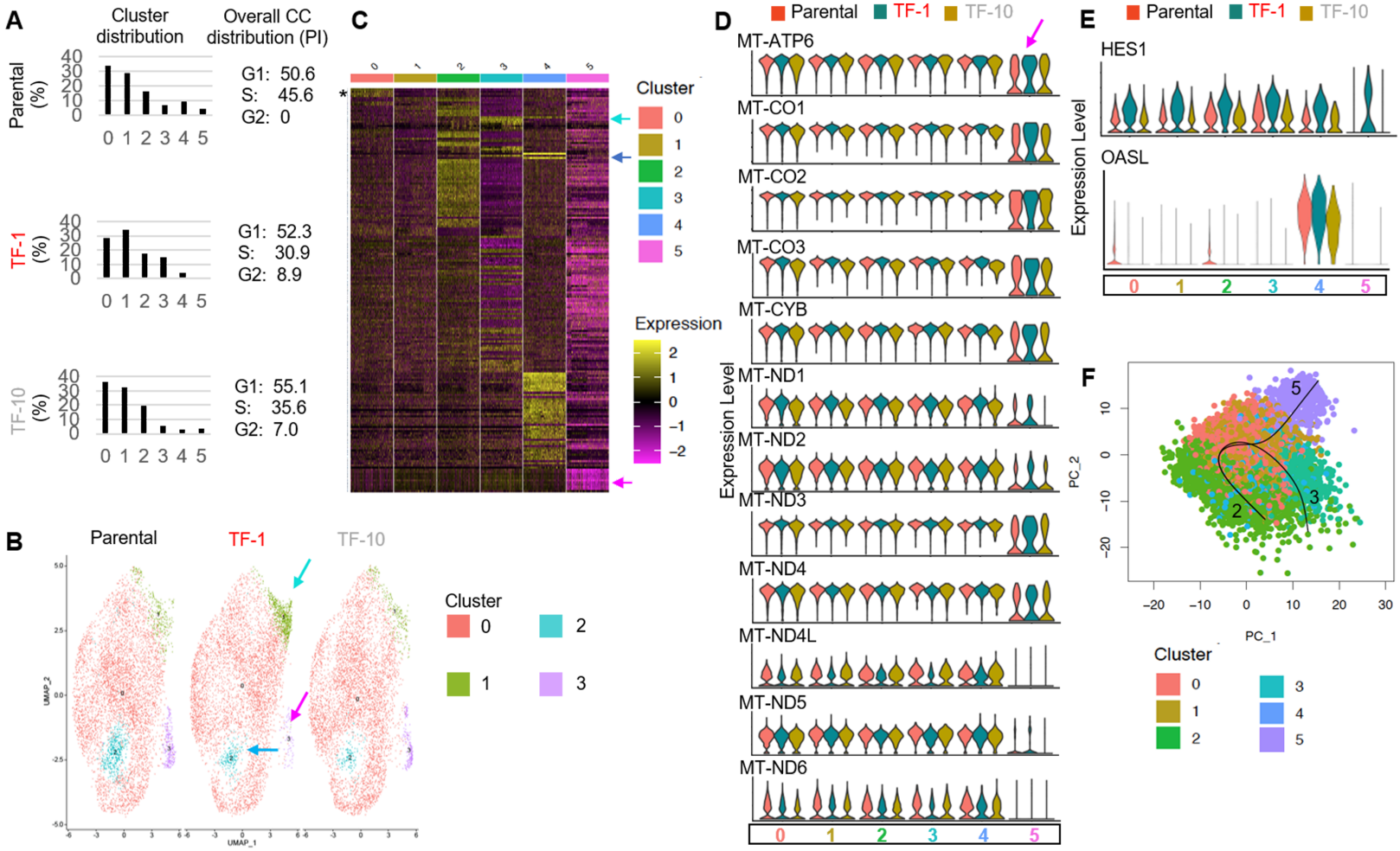

Extended Fig. 2

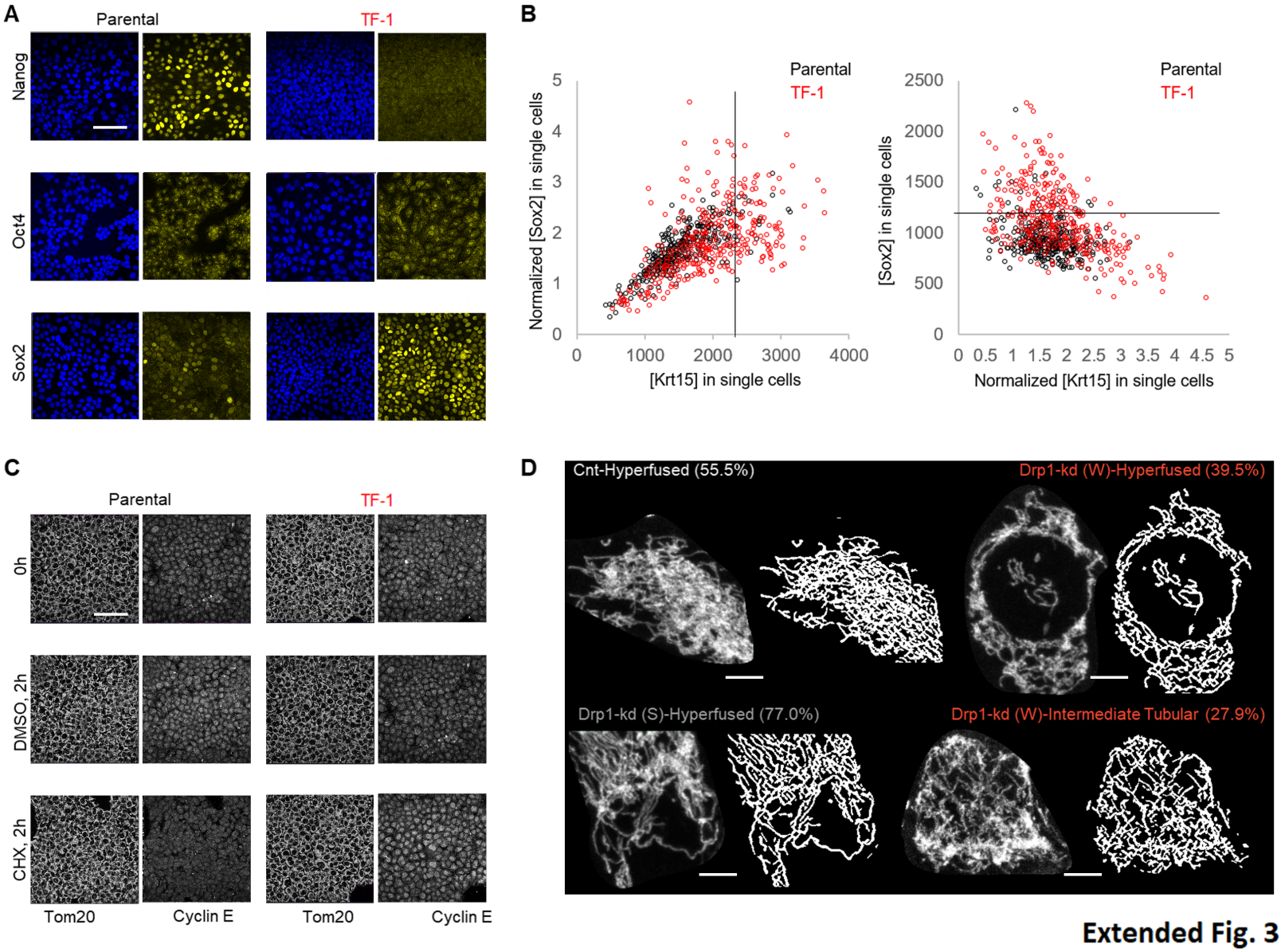

Extended Fig. 3

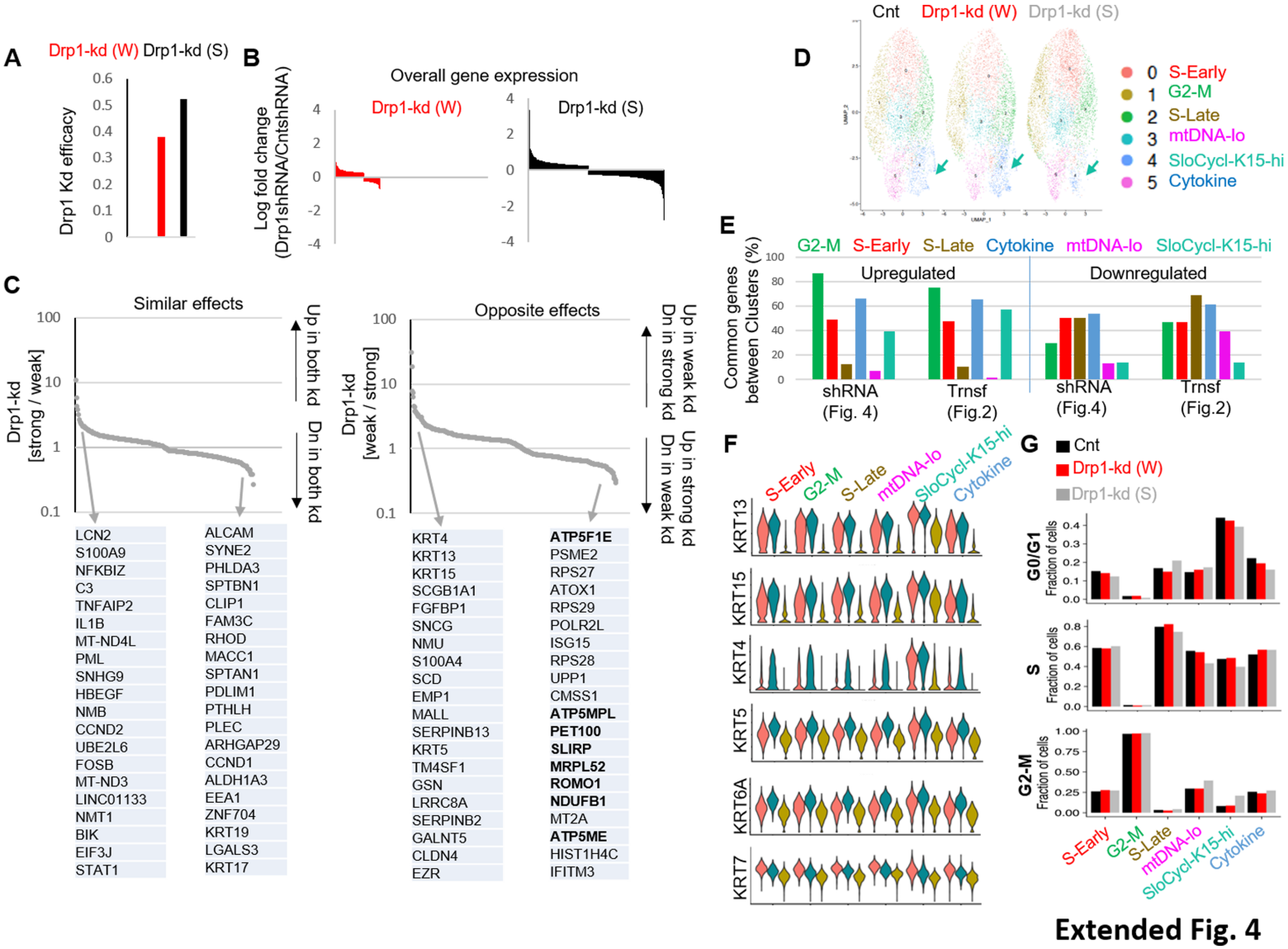

Extended Fig. 4

EXTENDED FIGURE LEGENDS:

Extended Figure 1. A) Quantification of incidence and volume of xenograft tumors formed by TF-1 and TF-10 HaCaT cells; # indicates presence of a distant tumor. **B)** Immunoblot analyses of Cytochrome C, Fis1, Tom20 and actin (loading control) in Parental and TF-1 and TF-10 HaCaT cells.

Extended Figure 2. A) Bar plot showing the percentage distribution of the clusters (0-5) in each of the cell populations identified by scRNA-seq analyses of Parental, TF-1 and TF-10 HaCat cells (left); numbers show cell cycle distribution from flowcytometry analyses of PI stained cells in the corresponding population (right). **B)** UMAP plot of scRNA-seq derived clusters (0-5) of Parental, TF-1 and TF-10 HaCaT cells obtained with minimum cluster resolution; color coded arrows point the major change in cluster distribution in transformed cells. **C)** Heat map of statistically significant marker genes for the color-coded clusters (0-5) of Parental, TF-1 and TF-10 HaCaT cells; color coded arrows point to the top most marker gene in the 3 clusters that are have different distribution between the Parental and transformed populations; color index shows log fold change; * marks the Histone gene cluster. **D)** Violin plots depicting expression of the mt-DNA genes in the named scRNA-seq derived cell clusters in the Parental, TF-1 and TF-10 HaCaT cells. **E)** Violin plots depicting expression of HES1 and OASL genes in the named scRNA-seq derived cell clusters in the Parental, TF-1 and TF-10 HaCaT cells. **F)** PCA plot of trajectory analyses of the scRNA-seq derived cell clusters in the Parental, TF-1 and TF-10 HaCaT cells.

Extended Figure 3. A) Representative confocal micrographs of immunostained Parental and TF-1 HaCaT cells showing endogenous expression of Oct4, Nanog and Sox2; blue depicting nuclear staining with Hoechst. **B)** Dot plot of [Sox2] and [Krt15] obtained from confocal micrographs of co-immunostained Parental and TF-1 HaCaT cells; [Sox2] levels normalized to the minimum in the respective population (left) and [Krt15] levels normalized to the minimum in the respective population (right); black lines demarcate levels of Sox2 and Krt15 as determined from the normalized signal of the other. **C)** Representative confocal micrographs of Parental and TF-1 HaCaT cells showing endogenous expression of Tom20 and Cyclin E1 after 2 hours incubation with

DMSO or Cychloheximide, with the pre-incubation time point (0h) as control. **D)** Representative maximum intensity projections (MIP) of confocal optical sections (micrograph) and the corresponding MitoGraph generated binary images (binary) for quantifying [Fission] and [Fusion1/5] metrics of the Parental HaCaT cells expressing non-targeted shRNA (Cnt), strong (S) or weak (W) Drp1 shRNA; the cells represent populations in colored boxes in Fig. 4A while the number depicts their abundance in percentage. Scale bar depicts 100 μm (A, C) or 15 μm (D).

Extended Figure 4. A) Bar plot showing the knockdown efficiency of strong (S) or weak (W) Drp1 shRNA expressed as ratio of Drp1 transcript levels in the knockdown HaCaT and that of the cells expressing the non-targeted shRNA control. **B)** Bar plot showing log fold change of overall gene expression of Parental HaCaT cells expressing strong (S) or weak (W) Drp1 shRNA with respect to those expressing the non-targeted shRNA (Cnt). **C)** Plots showing ratio of the expression of covered genes between the Parental HaCaT cells expressing strong (S) or weak (W) Drp1 shRNA; “Similar effects” showing ratio of increase or decrease in the (S) Drp1 shRNA over the (W) Drp1 shRNA (back arrows in left panel), while opposite effects showing opposite trends in genes as labelled in the arrows (back arrows right panel); grey arrows point to the top 20 genes of each category. **D)** UMAP plot of scRNA-seq based clusters (0-5) of Parental HaCaT cells expressing non-targeted shRNA (Cnt), strong (S) or weak (W) Drp1 shRNA; arrow pointing the SloCyc-Krt15-hi cluster (note color coding is not same as the one presented in Fig. 2). **E)** Bar plot showing percentage of statistically significant common genes (Upregulated or Downregulated) between color coded clusters obtained with the scRNA-seq data set of parental and transformed HaCaT cells (Fig. 2) and that of parental expressing control or Drp1 shRNAs (Fig. 4); same color coding is maintained between the two data sets. **F)** Violin plots depicting expression of Krt13, Krt15, Krt4, Krt5, Krt6A, Krt7 genes in the named scRNA-seq based cell clusters in the Parental HaCaT cells expressing non-targeted shRNA (Cnt), strong (S) or weak (W) Drp1 shRNA. **G)** Bar plot showing fraction of cells in G2-M, S and G0/G1, computed from main Fig. 4G, in the functionally categorized clusters in the Parental cells expressing non-targeted shRNA (Cnt), strong (S) or weak (W) Drp1 shRNA.